Research Paper

Influence of different circumferential heat flux distributions on flow boiling of R245fa in a circular horizontal tube

A.T. Martin, J. Dirker [*]

Clean Energy Research Group, Department of Mechanical and Aeronautical Engineering, University of Pretoria, Pretoria, South Africa

A B S T R A C T

Direct steam (and vapour) generation in parabolic trough collectors remains practically untapped due to inherent multi-physics challenges. Such difficulties include an understanding of the effect the non-uniform solar flux has on the boiling flow within absorber tubes. For this purpose, steady-state flow boiling of R245fa was experimentally investigated in a 17.12 mm diameter horizontal stainless-steel tube, at a saturation temperature of 40 °C, and mass fluxes of 125 kg/m^{2}s to 300 kg/m^{2}s. Various circumferential heat flux distributions were considered at the same total heat rate, including fully uniform heating, bottom half heating, top half heating, side half heating, and a representative parabolic trough collector heating profile. Locally applied heat fluxes ranged from 0.38 kW/m^2 to 30.48 kW/m^2. It was found that the transition between flow patterns were not affected by the heat flux distribution. A stochastic inverse model based on Bayesian inference was developed to resolve the heat transfer coefficients. The heating profile significantly altered the heat transfer performance in terms of the local and average heat transfer coefficients. Relative to uniform heating, the average heat transfer coefficients ranged between approximately a 144 % enhancement to a 40 % reduction, depending on the heat flux distribution, mass flux, and vapour quality. The parabolic trough collector heating profile had the best average heat transfer coefficient for most conditions, whereas uniform heating demonstrated superior heat transfer coefficients for highly convective dominant flow. Locally resolved heat transfer coefficients identified the dominance of nucleate boiling at the tube's lower circumference. Existing predictive methods from literature were found unsuitable when applied at the local level. Further investigation is required to determine the relative dominance of convective and/or nucleate boiling at different circumferential positions.

1. Introduction

Concentrated solar power (CSP) provides a renewable and competitive carbon–neutral alternative to fossil-fuel technologies in meeting future energy demands [1,2]. Several CSP configurations exist, whereby the solar-to-thermal energy conversion is facilitated via the optical concentration of direct normal irradiation (DNI) onto a central receiver. The parabolic trough collector (PTC) is a mature and commonly employed CSP technology [3,4] that typically utilises a horizontal absorber tube as the receiver. Consequently, the fluid flowing within the absorber tube is brought to a high exergy state and can, for instance, be used in electrical power generation via a Rankine or organic Rankine cycle (ORC) [5]. This can either be done indirectly through an auxiliary heat transfer fluid that transports thermal energy from the absorber tube to a steam/vapour generator, or directly via the production of steam/vapour within the absorber tube, without the need of the intermediate heat transfer fluid system. The latter, referred to as direct steam generation (DSG) when water is used, promises increased thermodynamic efficiency and economic viability [5]. For fluids other than water, a more apt description is direct vapour generation (DVG) when employed in ORCs. ORCs, operating on refrigerants such as R245fa, have recently gained traction [6–8] due to their unique potential for low and medium-grade heat recovery [9,10]. This is of interest in scenarios with low solar irradiance [11] or when relatively low-temperature waste heat is available [12].

Although having innate advantages, the boiling phenomena introduced in the absorber tube makes for non-trivial challenges when modelling DSG and DVG. Furthermore, PTC tubes induce a large circumferential non-uniform heat flux (NUHF) on the boiling flow [13–16], which can cause significant thermally-induced deflections of the absorber tube if neglected, resulting in component failure and reduced optical efficiency [17,18]. Therefore, a fundamental understanding of the thermohydraulic characteristics of flow boiling under

Nomenclature

A	Surface area of heating sector [m^2]
a, b	Model coefficients [-]
Bo	Boiling number [-], $\left(Bo = \dot{q}/[G(h_g - h_l)]\right)$
C	Constant [-]
Co	Confinement number [-], $\left(Co = 1/D\sqrt{\sigma/[g(\rho_l - \rho_g)]}\right)$
c_p	Specific heat capacity [J/kgK]
D	Diameter [m]
Fr_l	Liquid Froude number [-], $\left(Fr_l = [(1-x)G]^2/(gD\rho_l^2)\right)$
g	Gravitational acceleration [m/s^2]
G	Mass flux [kg/m^{2}s], $(G = 4\dot{m}/\pi D^2)$
h	Specific enthalpy [J/kg]
I	Current [A]
L	Length [m]
$\dot{m}$	Mass flow rate [kg/s]
N	Number of data points [-]
Nu	Nusselt number [-], $(Nu = \alpha D/\lambda)$
P	Pressure [Pa]
P_A	Probability of annular flow [-]
$\boldsymbol{P}$	Unknown parameter vector [W/m^{2}K]
$\widehat{\boldsymbol{P}}$	Parameter vector point estimate [W/m^{2}K]
$p(\boldsymbol{P})$	Prior probability density function
$p(\boldsymbol{P}|\boldsymbol{Y})$	Posterior probability density function
$p(\boldsymbol{Y}|\boldsymbol{P})$	Likelihood function
$p(\boldsymbol{Y})$	Marginal probability
$\dot{q}$	Heat flux [W/m^2]
$\dot{Q}$	Heat rate [W]
r	Radius [m]
$\widehat{r}$	Thermocouple radial location [m]
R	Ohmic resistance [Ω]
Re_{go}	Gas-only Reynolds number [-], $\left(Re_{go} = GD/\mu_g\right)$
$\Re$	Parameter space [W/m^{2}K]
t	Time [s]
T	Temperature [°C]
ΔT	Temperature offset [°C]
V	Voltage [V]
We_{lo}	Liquid-only Webber number [-], $\left(We_{lo} = G^2 D/(\sigma\rho_l)\right)$
x	Vapour quality [-]
X_{tt}	Lockhart-Martinelli parameter [-], $\left(X_{tt} = (1-x/x)^{0.9}(\rho_g/\rho_l)^{0.5}(\mu_l/\mu_g)^{0.1}\right)$
Y	Corrected wall temperature [°C]
$\boldsymbol{Y}$	Data vector of measured wall temperatures [°C]

Greek symbols

α	Heat transfer coefficient [W/m^{2}K]
ϵ_E	Experimental measurement error [°C]
θ	Angle [°]
$\widehat{\theta}$	Thermocouple angular location [°]
λ	Thermal conductivity [W/mK]
μ	Dynamic viscosity [Ns/m^2]
ρ	Density [kg/m^3]
σ	Surface tension [N/m]
σ_E	Standard deviation of experimental measurement error [°C]
Ω	Tube wall domain [-]

Subscripts

cal	calculated
dp	differential pressure ports
exp	experimental
g	gas/vapour
h	heated
in	inner/inlet
l	liquid
m	Test-section station index
MAP	Maximum a posteriori (point estimate)
meas	measured
n	Heating element index
nb	nucleate boiling
out	outer/outlet
PH	Preheater
PP	Posterior predictive samples
sat	saturation
ss	stainless steel
tru	true
TS	Test section
uniform	uniform case
w	wetted wall

NUHF conditions is critical in the design and control of PTC systems with DSG and DVG, and similar NUHF flow boiling technologies.

Research pertaining to non-uniformly applied heat fluxes on fluid flow is comparatively lacking in literature and has largely been neglected in the analysis of PTC applications. Recently, numerical simulations have been used in studying PTC tubes under non-uniform solar flux distributions on single-phase fluids, including thermal oils [16], molten salts [19], carbon dioxide (CO$_2$) [15], and nanofluids [20]. Qiu, et al. [15] analysed supercritical CO$_2$ and found the temperature of the absorber tube to follow the non-uniform solar flux distribution, agreeing with experimental observations [17]. Symmetrical cross-sectional vortices were generated due to buoyancy induced secondary flow. Wang, et al. [19] found similar temperature distributions when modelling a PTC with molten salt flow. Huang, et al. [21] numerically studied fully developed turbulent mixed convection and found a PTC heat flux profile to induce buoyancy-driven secondary flow which significantly altered the thermohydraulic characteristics to that of a uniformly heated scenario. The heat transfer coefficient (HTC) values and friction factors mostly increased with the NUHF [21], and secondary flow was enhanced by increases in the Grashof number and decreases in the Reynolds number [21]. Okafor,

et al. [22] presented a numerical model for mixed convection laminar flow and showed buoyancy-induced secondary flow to significantly enhanced the HTC, increasing with heat flux intensity and angle span.

Several experimental studies have also investigated the influence of a NUHFs on single-phase flow. Buoyancy-driven secondary flow in horizontal square [23] and rectangular [24] channels with the bottom wall heated have been found to induce vortices, as plumes of warm fluid rise from the heated surface and cooler fluid drops. Chang, et al. [25] numerically and experimentally investigated turbulent water flow with semi-circumferential heating from above, noting the average HTC values were unaffected by the NUHF and were accurately captured by the Dittus and Boelter [26] correlation. Shen, et al. [27] experimentally investigated molten salt at unilateral heat flux ratios of 1, 2, and 5.7, where it was found the HTC values were stronger on the lower heat flux surface. Dirker, et al. [28] experimentally studied several NUHFs on water flow in the laminar-transitional regime and found the HTC to be significantly affected by the heat flux distribution and intensity. The NUHFs reduced the average HTC in comparison to uniform heating, while applying the heat flux to the bottom of the tube was superior to other semi-circumferential heat flux distributions [28].

Most of the efforts to understand the influence of a NUHF have thus far been limited to single-phase flow and have yet to significantly consider the additional complexities of two-phase flow, such as saturated flow boiling within DSG and DVG applications. The introduction of two-phase flow causes for various liquid–vapour geometric flow structures to evolve, which has been coined flow patterns. The flow patterns are intrinsically linked to the thermohydraulic characteristics of boiling flow and have thus seen considerable attention. In general, saturated flow boiling has been accepted to constitute both nucleate boiling and convective boiling heat transfer mechanisms. Several methods have been proposed on how to model these interlinking mechanisms, with a comprehensive review given by Fang, et al. [29]. While refrigerant flow boiling has been extensively studied over the past several decades, there is a lack of experimental research on non-uniform heating conditions and tube diameters in the order of tens-of-millimetres [30], such as those employed in PTC and waste-heat recovery systems. This is particularly true for R245fa, which is a popular ORC fluid [31], where little attention has been given to diameters greater than 10 mm. Kaya, et al. [30] provided an isolated study investigating R245fa in a 21 mm diameter tube at high reduced pressures. However, the results remained exclusive to uniformly applied heat fluxes.

Lobón, et al. [32] numerically investigated a DSG-PTC facility with a NUHF boundary condition and developed a robust computational fluid dynamics model, which was later extended for transient conditions [33]. The results were in good agreement with solar test facility data [34]. Stratified flow boiling in an absorber tube was numerically modelled by Pal and Ravi Kumar [35]. The calculated HTC values had a notable circumferential non-uniformity, attributed to the phase asymmetry in stratified flow (liquid accumulation at the lower tube circumference) and the poor heat transfer capacity of the vapour phase.

Peatiwala and Boyd [36] experimentally investigated subcooled flow boiling in vertical tubes with semi-circumferential heating. Fang, et al. [37] accounted for three-sided heating in rectangular-channel flow boiling by calculating the heat flux based on an effective heat transfer area. Weise, et al. [38] experimentally investigated CO_2 flow boiling with circumferential varying heat fluxes at constant wall temperatures. The local heat flux was found to be fundamental in accurately predicting the nucleate boiling contribution, while the pool boiling correlation of Cooper [39] required no suppression factor as recommended in earlier work [40]. Wang, et al. [41] recently investigated R245fa flow boiling in a 10 mm diameter tube, with semi-circumferential bottom heating. The average HTC was enhanced via a strengthened nucleate boiling mechanism from the increased heat flux of the non-uniform distribution. However, direct comparisons to the uniform heat flux results were absent. Dirker, et al. [42] experimentally investigated several NUHFs on annular flow boiling of R245fa in a horizontal 8.5 mm diameter tube. The NUHFs significantly reduced the average HTC in comparison to uniform heating, where deviations increased with vapour quality. However, flow pattern data was not captured, and the effective heat transfer mechanisms remained speculative.

Based on existing literature, there are a limited number of experimental studies on NUHF flow boiling, and more specifically at larger tube diameters that is of interest to DSG and DVG industrial applications. Furthermore, the work that has been conducted on smaller tube diameters (<10 mm) remains incomplete, with minimal locally resolved detail and has yet to acknowledge the thermohydraulic mechanisms of the liquid–vapour flow structure. In the work that is reported on here, the aim was to experimentally investigate saturated flow boiling of R245fa in a horizontal tube with a larger diameter (>10 mm), with particular interest on the effect of circumferential NUHFs. Internal flow patterns were visually captured to provide a fundamental understanding of the underlying heat transfer mechanisms at the local and average level. A comparison to uniform heating was conducted with several NUHF profiles, including a PTC heating profile – which has not yet been conducted in literature. The trends and observations with R245fa might also be insightful for cases using other fluids.

2. Experimental apparatus

2.1. Facility

The experimental facility, as depicted schematically in Fig. 1, comprised of a primary closed refrigerant loop operated with oil-free R245fa. Heat addition occurred electrically, while an auxiliary cooling-water circuit was used to remove heat. Adopted from Dirker, et al. [43], the facility underwent extensive modifications and was fully recommissioned for the current experimental investigation.

A magnetically coupled speed-controlled GATHER gear pump (maximum flow rate of 540 L/h) was used to circulate refrigerant through the flow loop. Prior to the pump, an 18 L receiver tank which was elevated 1.5 m above the pump's suction inlet maintained a constant supply of subcooled liquid that was passed through a filter drier before being pumped to the rest of the system. Besides the separation of the phases, the receiver tank further acted as a thermal buffer.

After the pump, the majority of the fluid passed through Path A to the flow boiling test section, while a portion bypassed back to the receiver tank via Path B. This enabled improved flow stability and allowed for finer control and adjustment of the test-section mass flow rate via an inline needle valve. Consequently, the gear pump and needle valve were simultaneously responsible for setting the test section's saturation pressure and mass flow rate. Depending on the operating condition, the mass flow rate was measured by one of two Micro Motion™ ELITE™ Coriolis flow meters (CMFS010 or CMFS025). The maximum operational capacities were 110 kg/h and 2100 kg/h, respectively, with an accuracy of 0.1 % of the full scale.

Two in-series electrically powered preheaters were used to control the inlet vapour quality to the test section. Each preheater constituted an 11 mm inner diameter (ID) copper tube, 1.9 m in length, uniformly heated via spirally wound, electrically insulated constantan resistance wire. The electrical resistance of each preheater was 25 Ω and saw a connection to its own dedicated 3 kW Elektro-Automatik EA8360-30 DC power supply unit, with a maximum output of 360 V and 30 A ($\leq$ 0.2 % accuracy of the nominal value).

Next, the fluid at the controlled state entered the test section, which was also electrically heated. The test section allowed for different circumferential heat flux profiles to be applied, and enabled the resulting thermal response to be recorded, as will be discussed in further detail later.

Following the test section, the fluid was subcooled by a water-cooled fluted tube-in-tube condenser, with a maximum rated capacity of 72 kW. The condenser extracted thermal energy from the system and was instrumental in controlling the system pressure. It was serviced by $\sim$ 5 °C water from an auxiliary, externally controlled, chiller unit. An Ebara 90 centrifugal pump circulated the chilled water, while a Honeywell® three-way valve controlled the mass flow rate to the condenser. The resulting water mass flow rate was measured by a Micro Motion™ ELITE™ Coriolis flow meter CMFS025, with a maximum operational capacity of 2100 kg/h and an accuracy of 0.1 % of the full scale. Thereafter the refrigerant was returned to the receiver tank, completing the flow loop.

To reduce heat loss to (or gain from) the laboratory, the complete facility was thermally insulated with Armaflex insulation, with a thermal conductivity of 0.034 W/mK and a minimum thickness of 65 mm.

For monitoring and control purposes, the facility was instrumented at several sensing locations with thermocouple stations (symbol T in Fig. 1), resistance temperature detectors (RTDs) (symbol RTD in Fig. 1), and pressure sensors (symbol P in Fig. 1). Each thermocouple station consisted of four T-type thermocouples (0.1 °C accuracy) equispaced around the tube's circumference and secured to the outer surface via Kapton tape. The RTDs were OMEGA™ 1/10 DIN Pt100s (0.06 °C accuracy) mounted axially within the fluid flow. The pressure sensors before and after the gear pump were Gems® 2200 series gauge pressure transducers, with a pressure range of 2 MPa (accuracy of 0.15 % of the
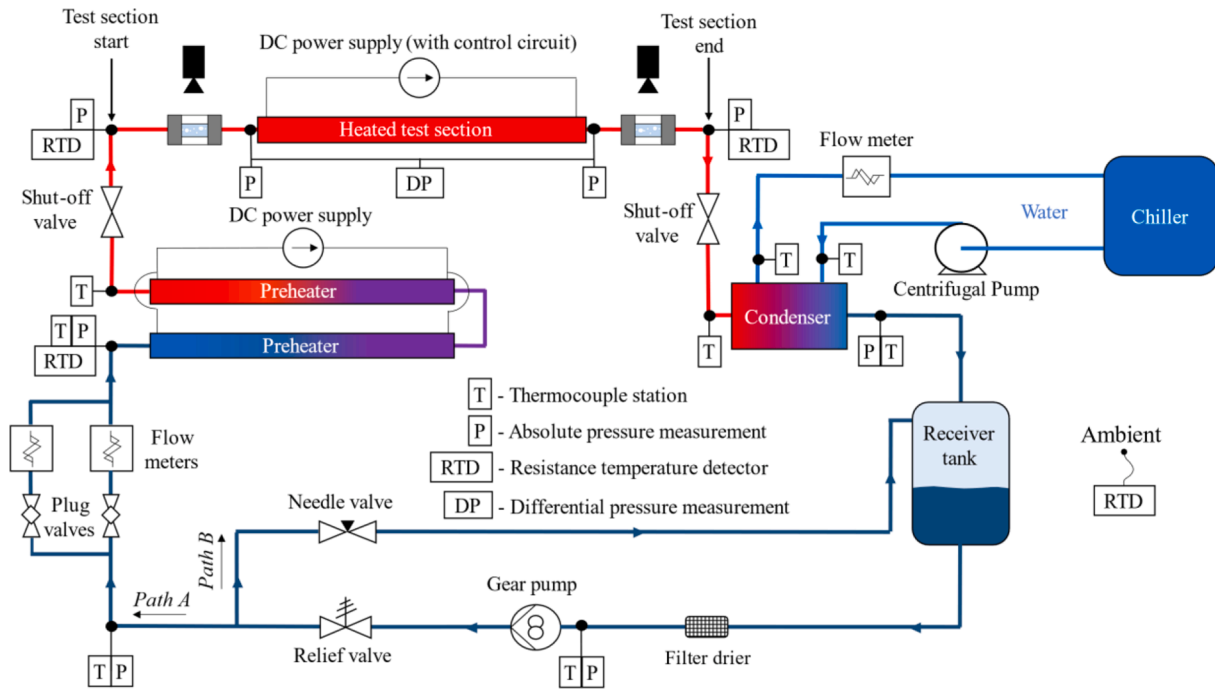
Fig. 1. Schematic of the experimental facility and instrumentation (not to scale).

full scale). The remaining pressure sensors were Honeywell® Sensotec® FP2000 gauge, with a pressure range of 3.45 MPa (accuracy of 0.1 % of the full scale). The pressure sensors were mounted horizontally and perpendicular to the fluid flow via 0.8 mm holes in the tube wall. To prevent flow disturbances, the holes were smaller than 10 % of the tube's ID and were carefully deburred.

2.2. Test section

The test section, which is depicted schematically in Fig. 2, consisted of an adiabatic calming length, an inlet sight glass, a heated length, and an outlet sight glass. All test section lengths (excluding the sight glasses) were constructed from a seamless 316L stainless steel tube with a thermal conductivity (λ_{ss}) of 14.11 W/mK [44], an outer diameter (OD) of 21.34 mm (D_{out}), an ID of 17.12 mm (D_{in}), and a measured surface roughness of 1.43 μm. The relatively low thermal conductivity of stainless steel allowed for better circumferential retention of non-uniform heat flux distributions. As in the facility, the test section was insulated with Armaflex (thickness of 70 mm). The worst-case heat loss was estimated by a thermal resistance network to be less than 1 %.

The calming length of 60 IDs was employed at the entrance of the test section to attenuate flow disturbances from upstream bends and entrance effects. The selected length was based on the findings of Cho and Tae [45], which showed the influence of a U-bend on downstream HTC diminished after 48 IDs.

The sight glasses provided non-intrusive optical access to the flow patterns before and after the heated length. Borosilicate glass tubes 70 mm in length were used, and a near seamless transition was achieved by matching the IDs of the glass tube to the stainless-steel tube.

A horizontally mounted Photron FASTCAM Mini UX100 high-speed digital camera with a Tokina 100 mm f/2.8 macro lens was used to record the liquid–vapour flow patterns at the sight glasses at 2000 frames per second, a resolution of 1280 × 616, and a shutter speed of 125 μs. Additional backlighting was employed via a light emitting diode.

The stainless-steel tube (Fig. 2 (a)) had a heated length of 1000 mm (L_h). Eight circumferential heating elements ($n = 1$ to 8) spanning 45° each (Fig. 2 (b)) were attached to the outer diameter and could be powered and controlled independently to produce several heat flux

distributions. The circumferential position around the tube is indicated by angle θ, with 0° indicating the bottom. Each heating element consisted of four parallel-running constantan resistance wire passes which had an Ohmic resistance of 15 Ω at a rated uncertainty of 1 %. The wire was 0.38 mm in diameter and had a 0.2 mm PFA electrically insulative sleeve. To ensure uniform thermal contact resistance with the outer surface of the tube, the wire passes were secured by tightly wrapped Kapton tape. Additional compression was provided via clamps axially spaced at 50 mm intervals. A polyvinyl chloride compressive plate (~0.1 W/mK) acted to uniformly distribute the compressive load and provide a thermal resistance between the wire passes and clamps. In addition to the individual control over each heating sector, the tube was also operated in one of two rotational orientations, as depicted in Fig. 2 (c). By rotation of the tube, orientation (i) had heating element 1 spanning for $\theta \in [-45°; 0°]$ and orientation (ii) had heating element 1 spanning for $\theta \in [-22.5°; +22.5°]$, for reasons that will be discussed in more detail later.

The heating elements ($n = 1$ to 8) were powered by a 3 kW Elektro-Automatik EA8360-30 DC power supply unit, with a maximum output of 360 V and 30 A (≤ 0.2 % accuracy of the nominal value). The high-side voltage potential was set by the power supply unit, while the current flowing through each heating element was controlled via a dedicated common-emitter bipolar junction transistor amplifier device. The resulting low-side voltage potential of each heating element was measured via a bespoke voltage measurement device, with an uncertainty of < 0.09 % of the measured value.

A total of 80 T-type thermocouples with an accuracy of 0.1 °C were installed in the tube wall (Fig. 2 (b)). The probes were organised in groups of 10 stations ($m = $ A to J in Fig. 2 (a)) along the heated length, 100 mm apart. Each station consisted of 8 thermocouples positioned midway across the width of each heating element. The thermocouple junctions were embedded in the tube wall via a 1 mm diameter blind hole, machined to a depth of 1.5 mm (±0.1 mm). This resulted in an approximate mean junction depth of 1.05 mm. Arctic Silver® thermal adhesive with a thermal conductivity of ~ 7 to 9 W/mK was used to secure the thermocouple junctions in place.

Two pressure ports located symmetrically about the heated section and spaced 1009 mm (L_{dp}) apart, allowed for the saturation and
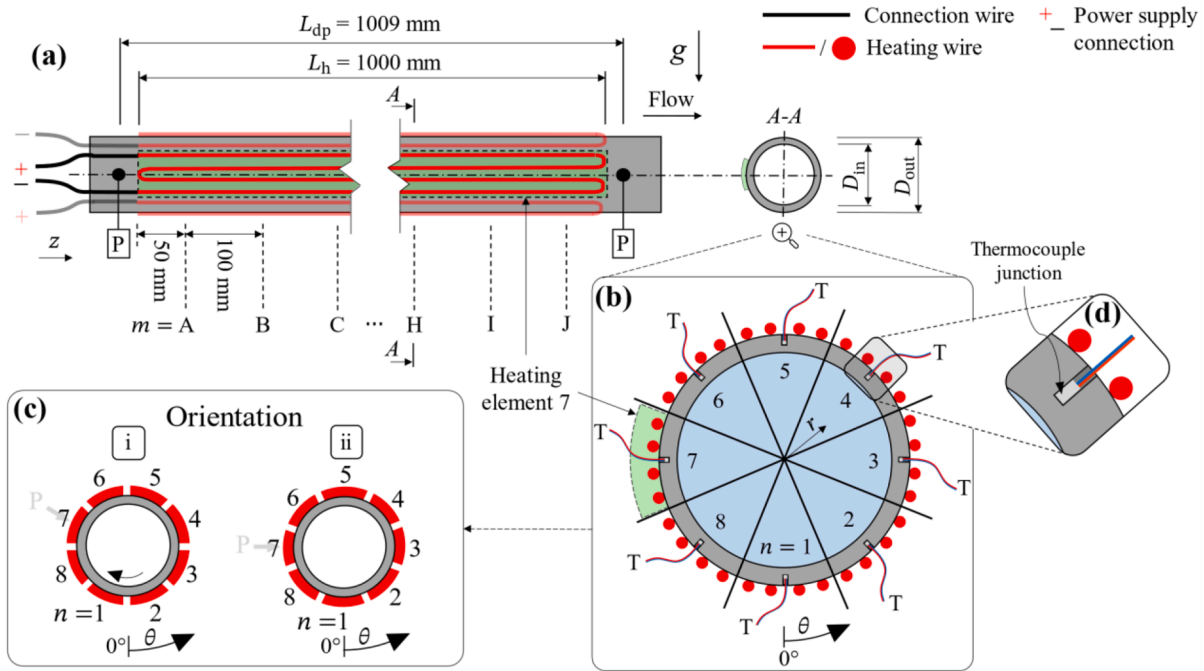
Fig. 2. Schematic of the heated test section (a) with axial measuring stations A to J, (b) cross-sectional view *A-A* displaying the circumferential heating sector notation, (c) tube orientations, and (d) a detailed close-up view of the wall and embedded thermocouple (not to scale).

differential pressures to be measured. The pressure ports were made by drilling a 1 mm diameter through hole ($<$10 % of the ID) and underwent post-manufacturing inspection to ensure there were no internal burrs. Honeywell® Sensotec® FP2000 pressure transducers (accuracy of 0.1 % of the full scale) were used to measure the absolute pressures at the inlet and outlet. In addition, a Validyne DP15 with a 14 kPa sensor diaphragm (uncertainty of 0.5 % of the full scale) was used to measure the differential pressure between the pressure ports.

2.3. System control and data acquisition

A personal computer (PC) coupled with a National Instruments LabVIEW environment was employed for system control and monitoring. The experimental instrumentation interfaced with a PC-connected National Instruments data acquisition system, consisting of a SCXI-1001 chassis and accompanying hardware. The power supplies and test-section current control device interfaced directly with the PC. Critical components were selected for manual control for safety purposes, including the refrigerant gear pump (via a GATHER control box) and the needle valve of the by-pass line.

3. Experimental methodology

3.1. Calibration and commissioning

The Pt100s and facility thermocouples were calibrated in a Lauda Proline water thermostat against two Lauda DigiCal DCS 2 digital thermometers with an uncertainty of 0.03 °C. The test-section thermocouples were calibrated in situ by passing highly turbulent liquid refrigerant flow through the flow loop at different steady-state temperatures. The reference temperatures were obtained from the Pt100 probes before and after the test section. The Honeywell® Sensotec® FP2000 pressure transducers were externally calibrated and the Gems® 2200 pressure transducers were calibrated against a WIKA CPT6400 pressure sensor with an uncertainty of 0.025 %. The Validyne DP15 pressure sensor was calibrated ex situ with a water column. The test-section heating elements' low-side voltage measurement device was

calibrated ex situ against a digital multimeter with an accuracy of $<$ 0.05 %.

The system was evacuated to 100 Pa (absolute pressure) before charging it with R245fa. The refrigerant purity was confirmed by comparing the measured saturation conditions to that of the thermophysical property library, CoolProp [46].

3.2. Test matrix

Table 1 gives a summary of the test conditions which covered a saturation temperature (T_{sat}) of 40 °C, mass fluxes (G) between 125 kg/m^{2}s and 300 kg/m^{2}s, and test-section inlet vapour qualities (x_{in}) of 0 to 0.8 at increments of 0.05. These target inlet vapour qualities were pre-defined and attained by adjusting the power input to the pre-heater for each operating mass flow rate. The actual inlet vapour qualities (which were within 0.01 from the target value) were checked by considering the experimental conditions and measured quantities as are described later in this paper. The saturation temperature was chosen to be as close to the evaporation temperature of ORC's, while remaining within the facility constraints. The test cases are plotted in Fig. 3 on the flow pattern map of Wojtan, et al. [47], adjusted for R245fa.

A variety of heat flux distributions were employed, as illustrated in Fig. 4 (a) and described in Table 2. These included: fully uniform heating (Case I), bottom half heating (Case II), top half heating (Case III), side half heating (Case IV), and PTC profile heating (Case V). In all cases the test section's total heat transfer rate ($\dot{Q}_{TS}$) of 650 W was chosen by considering a typical DNI of $\sim$ 630 W/m^2 and a PTC geometric concentration ratio of 20. Furthermore, the PTC profile (Case V) was

Table 1
Test matrix.

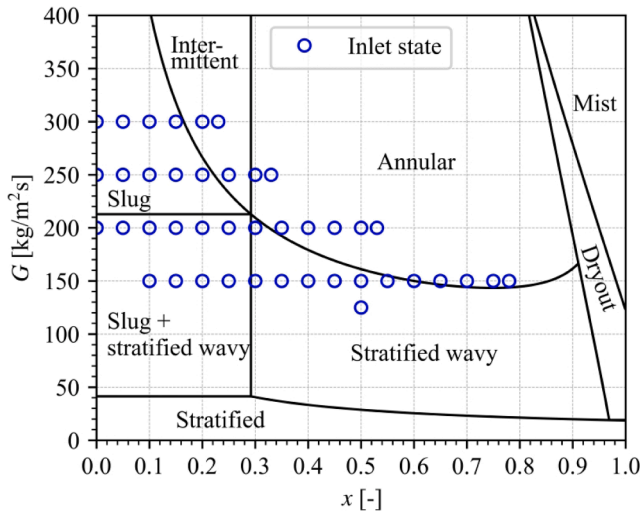| Parameter	Value (allowable deviation)
T_{sat} [°C]	40 ($\pm$0.5)
G [kg/m^{2}s]	125, 150, 200, 250, 300 ($\pm$3 %)
x_{in} [-]	0 – 0.8 ($\pm$0.01)
$\dot{Q}_{TS}$ [W]	650 ($\pm$0.5 %)
Heat flux profile	I, II, III, IV, V (Fig. 4 (a))

Fig. 3. Experimental test conditions presented on the flow pattern map of Wojtan, et al. [47].

obtained by discretising the LS-2 PTC profile [48] into 8 discrete sectors, and employed via orientation (ii) of Fig. 2 (c). The resulting local concentration ratios are compared in Fig. 4 (b). The particular shape of the heat flux profile is due to a PTC's large reflector mirror that reflects DNI toward the central absorber tube. Consequently, a high heat flux evolves on the bottom of the tube where the DNI is concentrated, whilst a lower heat flux evolves toward the top of the tube, due to the absence of the concentrated DNI. The local reduction of the heat flux towards the 0° circumferential position is due to the self-shadowing effect of the collector tube.

For each test case, steady state data was recorded via the LabVIEW interface at 10 Hz for 1200 samples, when the variation in the mass flow rates, inlet vapour quality, temperatures, and overall system energy balance error remained within 3 %, 1 %, 0.1 °C, and 2 %, respectively, for a 10-minute period.

4. Data processing

4.1. Image processing

The image processing of the inlet and outlet flow patterns followed a similar method to that proposed by Charnay, et al. [49] and Moran [50], whereby a mean greyscale intensity (MGI) signal was derived. First, the
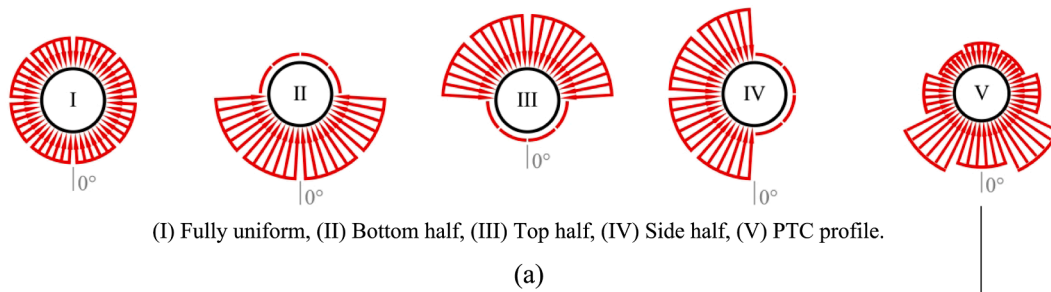
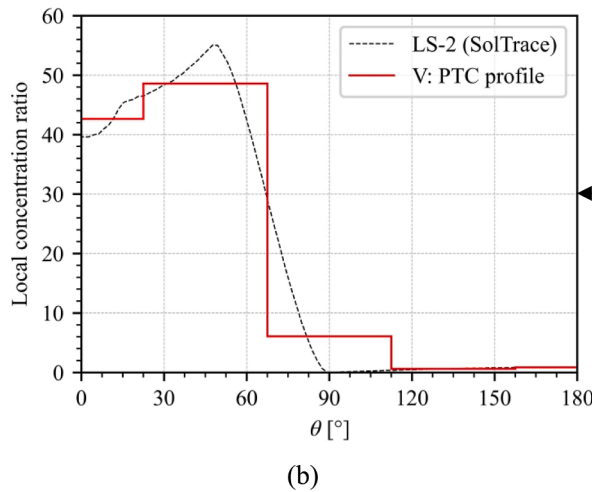(I) Fully uniform, (II) Bottom half, (III) Top half, (IV) Side half, (V) PTC profile.

(a)

(b)

Fig. 4. (a) Heat flux profile cases at a total heat rate of 650 W and (b) the heat flux profile of Case V.

Table 2
Locally applied heat flux per heating sector ($n = 1$ to 8).

Heat profile case		Orientation (Fig. 2 c)	Locally applied heat flux per heating sector [kW/m^2]							
			1	2	3	4	5	6	7	8
I:	Fully uniform	i	12.09	12.09	12.09	12.09	12.09	12.09	12.09	12.09
II:	Bottom half	i	24.17	24.17	24.17	0	0	0	0	24.17
III:	Top half	i	0	0	0	24.17	24.17	24.17	24.17	0
IV:	Side half	i	0	24.17	24.17	24.17	24.17	0	0	0
V:	PTC profile	ii	26.76	30.48	3.82	0.38	0.55	0.38	3.82	30.48

videos were converted to a greyscale equivalent, where each pixel had a greyscale value between 0 and 255. A region of 10 pixels wide and a hight equivalent to the tube's ID was selected at approximately the centre of the sight glass. For each video frame, the MGI was produced by averaging the greyscale values over the selected region. The process was finalised by normalising the MGI signal. Single-phase liquid and vapour regions were presented by near-white pixels (MGI $\approx$ 1), while phase interfaces produced near-black pixels (MGI $\approx$ 0). Consequently, the captured MGI signals were analysed to determine the frequency and duration of temporal variations in the liquid–vapour geometric flow structure, eliminating the subjective nature of pure visual inspection.

4.2. Test section fluid states

The actual inlet vapour quality to the test section was determined via the specific enthalpy of the inlet fluid (h_{in}):

$$x_{in} = \frac{h_{in} - h_l}{h_g - h_l} \tag{1}$$

where h_l and h_g are the saturated liquid and saturated vapour specific enthalpies, respectively, computed by CoolProp [46] at the average of the measured saturation pressures (P_{sat}) from the inlet and outlet pressure transduces. Realising the negligible heat loss over the insulated fluid line between the preheater's outlet and test section's inlet, and performing an energy balance over the preheater, the inlet specific enthalpy was calculated as:

$$h_{in} \approx h_{PH,out} = h_{PH,in} + \frac{\dot{Q}_{PH}}{\dot{m}} \tag{2}$$

Here, $h_{PH,out}$ is the preheater's outlet specific enthalpy, $\dot{m}$ is the mass flow rate, $\dot{Q}_{PH}$ is the total heat input rate at the preheater ($\dot{Q}_{PH} = VI$) based on the measured voltage (V) and electrical current (I) of the power supply, and $h_{PH,in}$ is the preheater's inlet specific enthalpy obtained from the measured pressure and temperature via CoolProp [46].

Each heating element ($n = 1$ to 8) of the test section had a heat input rate ($\dot{Q}_n$) given by Ohm's Law:

$$\dot{Q}_n = \frac{V_n^2}{R_n} \tag{3}$$

were R_n is the Ohmic resistance and V_n is the measured voltage potential. The test section's total heat input rate was given by the summation of individual heat rates, $\dot{Q}_{TS} = \sum_{n=1}^{8} \dot{Q}_n$. By using the steady-state energy balance over the test section, the outlet specific enthalpy (h_{out}) was calculated as follows:

$$h_{out} = \frac{\dot{Q}_{TS}}{\dot{m}} + h_{in} \tag{4}$$

which allowed the outlet vapour quality (x_{out}) to be computed:

$$x_{out} = \frac{h_{out} - h_l}{h_g - h_l} \tag{5}$$

From knowledge of the axially uniform heat input rate of the test section, the vapour quality (x) along the test section scaled linearly between x_{in} and x_{out}, with the average vapour quality ($\overline{x}$) calculated as the arithmetic mean of x_{in} and x_{out}. The local and average vapour qualities were used when evaluating the local and average heat transfer coefficients, respectively.

4.3. Test-section thermocouple offset

Special attention was given to correctly interpret the measured test-section wall temperatures, because of the close proximity of the heating

wires to the thermocouple leads in the test section. Any secondary heat conduction effects in the thermocouple lead would result in an artificial elevation of the measured temperature at the thermocouple junction, above that of the actual wall temperature. For the alphanumerically indexed thermocouples (Fig. 2) with $m = A$ to J, the corrected wall temperature ($Y_{m,n}$) was expressed in terms of the measured wall temperature ($T_{meas,m,n}$) and some offset temperature value ($\Delta T_{m,n}$):

$$Y_{m,n} = T_{meas,m,n} - \Delta T_{m,n} \tag{6}$$

The behaviour of $\Delta T_{m,n}$ for each thermocouple was derived from several in-situ turbulent single-phase experiments that was constrained to the range of 0 – 50 W per heating element, to reduce the effect of buoyancy driven secondary flow. It was found that $\Delta T_{m,n}$ was linearly dependent on the locally applied external heat rate ($\dot{Q}_n$):

$$\Delta T_{m,n} = \begin{cases} a_{m,n}\dot{Q}_n + b_{m,n}, & if\ \dot{Q}_n > 0 \\ 0, & if\ \dot{Q}_n = 0 \end{cases} \tag{7}$$

The coefficients $a_{m,n}$ and $b_{m,n}$ were experimentally fitted for each thermocouple. The uncertainty introduced by Eq. (7) was resolved in the model fitting.

4.4. Heat transfer coefficients

The local heat transfer coefficient ($\alpha_{m,n}$) at each tube wall location (m, n) took the form of Newton's law of cooling:

$$\alpha_{m,n} = \frac{\dot{q}_{w,m,n}}{T_{w,m,n} - T_{sat}} \tag{8}$$

where $T_{w,m,n}$ and $\dot{q}_{w,m,n}$ are the local wetted-wall temperature and heat flux, respectively. From these, the test section's average and lengthwise-average heat transfer coefficients were computed as $\overline{\alpha} = (1/80)\sum_{m,n}\alpha_{m,n}$ and $\overline{\alpha}_n = (1/10)\sum_m\alpha_{m,n}$, respectively.

However, the wetted–wall boundary conditions were not directly measured and had to be treated as unknown parameters. Consequently, they had to be derived from the known externally applied heat rates ($\dot{Q}_n$) and observed in-wall temperatures ($Y_{m,n}$). Thus, a classical inverse heat conduction problem was realised, as will be discussed below.

4.4.1. Physics heat conduction model – Forward problem

Governing equations

The governing equation for heat conduction within the domain (Ω) of a solid body, without internal heat generation, and assuming homogeneous and isotropic thermophysical properties, is given by:

$$\rho c_p \frac{\partial T}{\partial t} = \nabla(\lambda\nabla T)\ in\ \Omega \tag{9}$$

where ρ, c_p, λ, and t denote the density, specific heat capacity, thermal conductivity, and time, respectively. For the test section tube wall with an inner radius r_{in}, outer radius r_{out}, $\lambda_{ss} \approx$ constant, negligible axial heat conduction, and steady-state conditions, Eq. (9) can be rewritten in cylindrical coordinates (r, θ) for any given cross-sectional $r - \theta$ plane (Fig. 2 b) along the test section length:

$$\frac{\partial^2 T}{\partial r^2} + \frac{1}{r}\frac{\partial T}{\partial r} + \frac{1}{r^2}\frac{\partial^2 T}{\partial \theta^2} = 0\ in\ \Omega \tag{10}$$

where $\Omega = \{r_{in} \leq r \leq r_{out}; 0^\circ \leq \theta \leq 360^\circ\}$ and the in-wall temperature field $T = T(r,\theta)$

Boundary conditions

The external surface heat flux was modelled by a Neumann boundary condition:

$$\dot{q}(r_{out}, \theta) = \frac{\dot{Q}_n}{A_n} = \lambda_{ss} \frac{\partial T}{\partial r}\bigg|_{r=r_{out}} \tag{11}$$

where $\dot{Q}_n$ is given by Eq. (3) and $A_n = (1/8)\pi D_{out} L_h$ is the external surface area of each heating sector.

For the purpose of the inverse problem, the inner surface convection boundary condition – thus the heat transfer coefficient – was assumed to be uniform over each 45° angle span of a heating element sector, and modelled by a Robin boundary condition:

$$\lambda_{ss} \frac{\partial T}{\partial r}\bigg|_{r=r_{in}} = \alpha_{m,n}[T(r_{in}, \theta) - T_{sat}] \tag{12}$$

Furthermore, a self-imposed boundary condition resulted from the cylindrical nature of the tube wall:

$$T(r, \theta) = T(r, \theta + 360°) \tag{13}$$

The finite difference method (FDM) was employed to computationally solve Eq. (10) to (13) in Python and was validated against Ansys® 2021 R1 Fluent. The domain was discretised with a hexahedral mesh with 4 and 24 cells in the radial and tangential directions, respectively. The selected mesh provided a good combination of computational efficiency and accuracy, as found from a mesh independency study. The resulting mesh and heating element sectors are represented in Fig. 5.

The preceding equations described the direct heat conduction model that resolves the temperature field $T(r, \theta)$ within the tube wall at each test-section station, given the known external heat rates $\dot{Q}_n$ and set of unknown heat transfer coefficients $\alpha_{m,n}$. Therefore, $T(r, \theta)$ could not be directly solved as there was a missing boundary condition, that being $\alpha_{m,n}$ in Eq. (12). In addition, there were discrete temperature field measurements at $n = 1$ to 8 locations within Ω for each test-section station m = A to J:

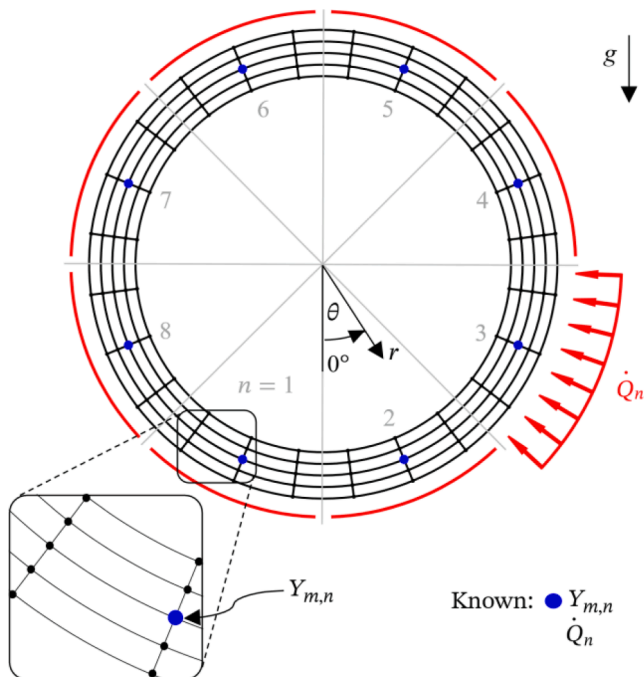$$Y_{m,n} \simeq T(\hat{r}_{m,n}, \hat{\theta}_{m,n}) \tag{14}$$

Fig. 5. Mesh of tube wall domain and heating sectors.

where $\hat{r}_{m,n}$ and $\hat{\theta}_{m,n}$ is the location of the respective thermocouple measurement, as indicated in Fig. 5, and $Y_{m,n}$ is the measured temperature at the defined location, given by Eq. (6). Therefore, the primary objective of the inverse problem was to find some set of inner surface heat transfer coefficients, such that the resolved temperature $T(\hat{r}_{m,n}, \hat{\theta}_{m,n})$ provided a suitable match to the measured temperature $Y_{m,n}$ at each thermocouple location. For this purpose, a Bayesian framework was adopted, providing a robust statistical technique to deal with the general ill-posed nature of inverse problems, while uniquely accounting for the uncertainties in the experimental measurements and providing statistical information on the resolved heat transfer coefficients.

4.4.2. Parameter estimation using Bayesian inference – Inverse problem

Bayes' theorem

Bayesian techniques recast inverse problems as statistical inference, with the aim of obtaining the posterior probability density function (PPDF) of unknown parameters. Considering the inverse heat conduction problem for each test-section station (m = A to J), the unknown parameter vector (P) comprises of the wetted-wall heat transfer coefficients:

$$P = [\alpha_{m,1}, \alpha_{m,2}, \alpha_{m,3}, \cdots, \alpha_{m,8}] \tag{15}$$

Given the measured wall temperatures, $Y = [Y_{m,1}, Y_{m,2}, Y_{m,3}, \cdots, Y_{m,8}]$, the PPDF can be described by Bayes' theorem:

$$p(P|Y) = \frac{p(Y|P)p(P)}{p(Y)} \tag{16}$$

where $p(P)$ is the prior probability density function, $p(Y|P)$ is the likelihood function, and $p(Y)$ is the marginal probability. Realising $p(Y)$ is a constant and generally difficult to compute, it is advantageous to rewrite the PPDF of Eq. (16) as the proportionality:

$$p(P|Y) \propto p(Y|P)p(P) \tag{17}$$

Likelihood

At each embedded thermocouple location $(\hat{r}_{m,n}, \hat{\theta}_{m,n})$, the measured wall temperature $Y_{m,n}$ (Eq. (6)) was known to present the true physical wall temperature ($T_{tru,m,n}$) with some additive experimental measurement error ($\epsilon_{E,m,n}$):

$$Y_{m,n} = T_{tru,m,n} + \epsilon_{E,m,n} \tag{18}$$

The experimental error was assumed to be normally distributed, with a zero mean and a variance of $\sigma_{E,m,n}^2$, which was known from the thermocouple measurement uncertainty. Furthermore, the true physical wall temperature was assumed to be perfectly predicted by the physics model of Eq. (10) to (13), since the errors induced by the FDM implementation were more than three orders of magnitude smaller than the experimental errors. Therefore, it was taken that $T_{tru,m,n} \approx T(\hat{r}_{m,n}, \hat{\theta}_{m,n})$. The likelihood function for each test-section station (m = A to J) was then calculated as follows:

$$p(Y|P) = \prod_{n=1}^{8} \frac{1}{\sqrt{2\pi\sigma_{E,m,n}^2}} \exp\left\{ -\frac{[Y_{m,n} - T(\hat{r}_{m,n}, \hat{\theta}_{m,n})]^2}{2\sigma_{E,m,n}^2} \right\} \tag{19}$$

Prior

The prior distribution is commonly used to regularise inverse problems, removing ill-posed conditions than may arise from experimental

errors and random noise. The prior provided a parameter space ($\mathfrak{R}$) over which the solutions to the inverse heat conduction problem can be explored. It was known the heat transfer coefficient could not be less than 0 W/m^{2}K and must be below some arbitrarily large heat transfer coefficient upper bound, which was chosen to be 10,000 W/m^{2}K. However, the probability distribution over the parameter space remained elusive. It has been common practice to use a uniform distribution over the parameter space so as to not inadvertently bias the posterior distribution. Therefore, the prior distributions were chosen as:

$$p(\boldsymbol{P}) = C, P \in R = [0, 10000] \, \text{W}/\text{m}^2 K \tag{20}$$

where C is a constant.

4.4.3. Evaluating the posterior probability density function with Markov chain Monte Carlo

Markov chain Monte Carlo (MCMC) provides a class of well-established numerical sampling techniques that can be used to evaluate the PPDF of Eq. (17). For this purpose, the No-U-Turn Sampler (NUTS) developed by Hoffman and Gelman [51] was implemented. The NUTS avoids the random-walk of the parameter space by using first-order gradient information from the likelihood function, while eliminating the need to hand-tune parameters as in Hamiltonian Monte Carlo.

The Python probabilistic programming framework PyMC [52] was used to implement the NUTS, creating a coherent FDM model and statistical inference package. The NUTS was implemented with four Markov chains at 5000 samples each, 1000 tuning steps, and a target acceptance rate of 0.8. The four independent Markov chains were initialised at different points within the parameter space and confirmed to converge to the same distribution. This ensured the correct parameterisation and confirmed the initialisation had no influence on the converged upon PPDF. An example of the typical sampling behaviour (4 × 5000 samples plotted in series) and resulting histogram plot from this study can be seen in Fig. 6, with qualitatively similar asymptotic behaviour seen for all parameter estimates. Notably, the four independent chains are indistinguishable in Fig. 6 (a), as they converged to the same distribution.

From the resulting PPDFs, the maximum a posteriori (MAP) was used as the heat transfer coefficient point estimates:

$$\alpha_{m,n=\{1,2,3,\cdots,8\}} = \widehat{\boldsymbol{P}}_{\text{MAP}} = \underset{\boldsymbol{P}}{\arg\max} \, p(\boldsymbol{P}|\boldsymbol{Y}) \tag{21}$$

whilst the 95 % credible interval evolved naturally from Bayesian inference. Fig. 6 (a) displays an example of the MAP and credible interval superimposed on the samples.
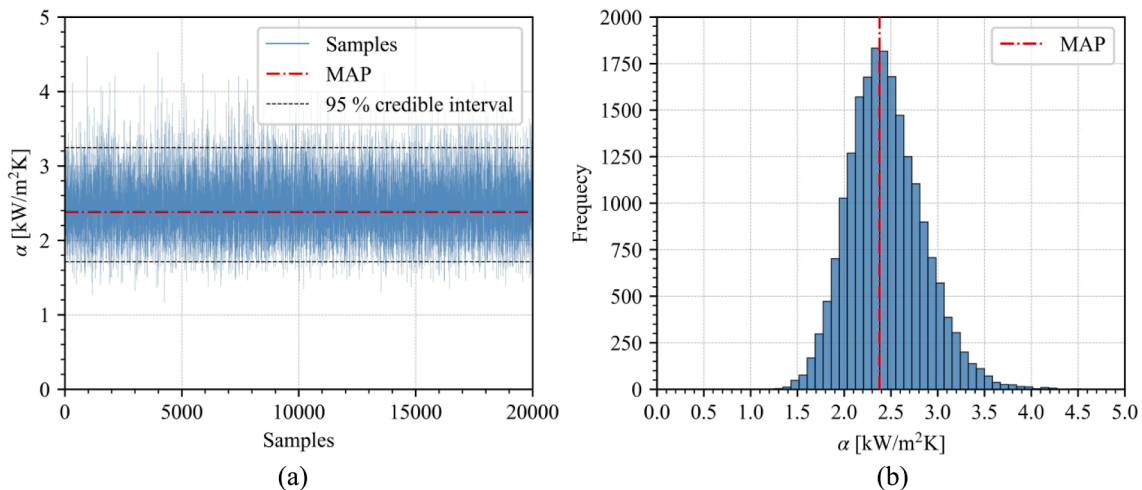
4.5. Uncertainty analysis

An uncertainty propagation analysis was conducted according to the method proposed by Moffat [53] for all parameters and values, except for the heat transfer coefficients, which evolved naturally from Bayesian inference. The 95 % confidence level uncertainties are summarised in Table 3.

5. Validation

5.1. Validation of the Bayesian inverse model

Although the Bayesian inverse model was verified against a deterministic problem of known values, it was valuable to also validate the model against experimental data. A representative example is considered here for flow boiling heat transfer with bottom half heating (Case II), for test-section station $m = $ C. Given the measured thermocouple temperatures and externally applied heat fluxes, the heat transfer coefficients were estimated via the inverse model of Section 4.4. The resolved heat transfer coefficients were then used to retrodict the temperatures at the thermocouple locations, as seen in Fig. 7. The predictive temperature estimates (Y_{MAP}) were in good agreement with the measured thermocouple temperatures, Y, where the scatter in the posterior predictive samples (Y_{PP}) indicated the associated uncertainties. The retrodicted temperatures can be seen to account for non-physical temperature deviations within the uncertainty bounds of the measurements. Fig. 7 allows one to visually intuit the performance of the inverse model, further validating the use of the Bayesian inverse model. Similar results were achieved for all other thermocouple locations.

Table 3
Uncertainty in the experimental parameters.

Parameter	Uncertainty	
	mode	min. – max.
$G\,[\text{kg}/\text{m}^2\text{s}]$	2.8 %	1.5 – 4.9 %
$x_{\text{in}}\,[-], \, x_{\text{out}}\,[-]$	0.009	0.009 – 0.03
$\bar{x}\,[-]$	0.007	0.007 – 0.02
$T_{\text{sat}}\,[°\text{C}]$	0.3 °C	0.3 – 0.4 °C
$P_{\text{sat}}\,[\text{Pa}]$	1.0 %	1.0 – 1.4 %
$T_{\text{w}}\,[°\text{C}]$	0.1 °C	0.07 – 1.9 °C
$\bar{\alpha}\,[\text{W}/\text{m}^2\text{K}]$	3.0 %	3.0 – 7.3 %
$\bar{\alpha}_n\,[\text{W}/\text{m}^2\text{K}]$	31.7 %	31.7 – 68.8 %
$\dot{q}_n\,[\text{W}/\text{m}^2\text{K}]$	2.8 %	2.8 – 4.2 %

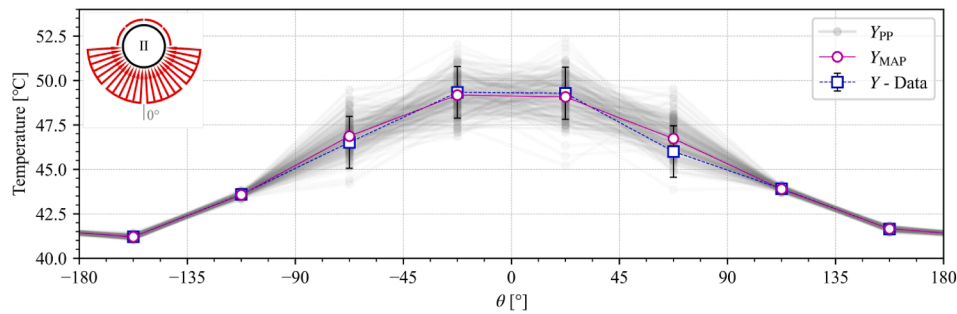**Fig. 6.** Example of the (a) sampling results and corresponding (b) histogram plot.

Fig. 7. Experimental and the retrodicted thermocouple wall temperatures for bottom heating.

5.2. Validation of experimental method and data analysis technique

A steady-state heat transfer validation was conducted on the test section with liquid R245fa at Reynolds numbers ranging between 11,000 to 24,000 (turbulent flow) and fluid temperatures of 15 °C and 30 °C. As displayed in Fig. 8, the average experimental Nusselt number (Nu_{exp}) was in satisfactory agreement with that calculated (Nu_{cal}) by the correlations of Gnielinski [54], Meyer, et al. [55], and Sieder and Tate [56], with a mean deviation of 0.8 %, − 3.9 %, and 2.1 %, respectively. Furthermore, the test-section energy balance error was within 0.86 %, supporting the negligible heat loss calculation.

There existed no flow boiling data in literature covering the current tube diameter and fluid of interest, therefore, requiring the flow boiling heat transfer validation to rely on a well-predicting correlation from literature. To ensure the most suitable alignment to correlations from literature (of different tube diameters and fluids), validation was restricted to annular flow under uniform heating, as it provided the most predictable liquid–vapour flow structure and has been well studied in literature. For this purpose, the flow-pattern based correlation of Woj-tan, et al. [40] was used to predict the annular flow heat transfer coefficient, as it has shown good results for macroscale tube diameters in annular flow of R245fa [43]. Steady-state flow boiling validation was conducted at $G = 150$ kg/m²s and 200 kg/m²s, and $T_{sat} = 40$ °C. Once annular flow was observed at the inlet and outlet sight glasses, an additional vapour quality increase of 10 % was set to ensure fully annular flow. Fig. 9 compares the calculated ($\bar{\alpha}_{cal}$) and experimental average ($\bar{\alpha}_{exp}$) heat transfer coefficients, which were in good agreement. The mean absolute deviation was 3.7 % and most data points fell within 10 % error.
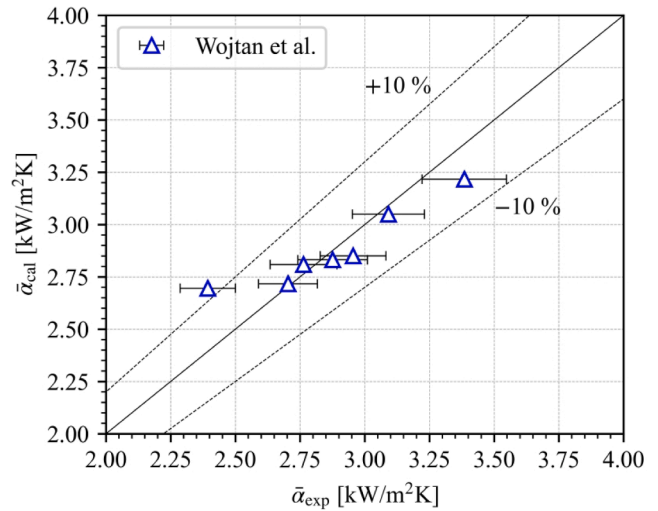

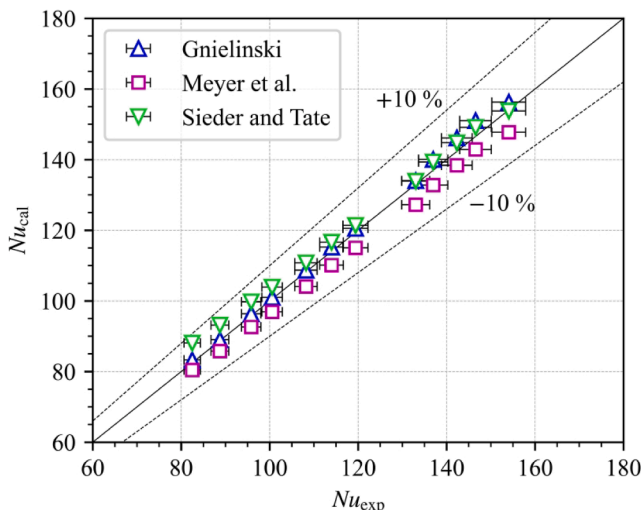**Fig. 8.** Single-phase heat transfer validation.

Fig. 9. Two-phase heat transfer validation.

6. Flow pattern

6.1. Flow patterns and MGI

Accurate knowledge of the flow pattern is highly desirable, as the thermohydraulic characteristics of flow boiling are intrinsically linked to the liquid–vapour flow structure. Some of the most prevalent flow patterns and their characteristic MGI signals of this study are presented in Fig. 10. These included: (a) plug flow, (b) slug flow, (c) stratified-wavy flow, (d) slug/stratified-wavy flow, (c) intermittent flow, and (f) annular flow.

Plug flow was characterised by a smooth vapour plug traversing the tube's upper surface, exclusively seen at the test-section inlet as $x \to 0$. Slug (S) flow had large spikes in the MGI as flow alternated between vapour bubbles and liquid slugs, intermittently wetting the tube's upper surface. Stratified-wavy (SW) flow was accompanied by a clear phase separation with interfacial ripples. Occasional liquid waves splashed up the tube wall, slightly spiking the MGI, while the upper surface remained dry. Slug/stratified-wavy (S + SW) flow was identified by stratified-wavy flow that was frequently interrupted by liquid slugs interfacing with the tube's upper surface. Intermittent (I) flow displayed chaotic and random fluctuations between various liquid–vapour flow structures, as captured by the MGI. Annular (A) flow had a constant liquid annulus surrounding a high-velocity vapour core, producing an approximately constant MGI, where the liquid film was thicker on the lower surface due to the influence of gravity. Ripples were almost always present on the liquid annulus, being identified as wavy-annular flow in literature [57]. The flow patterns agreed with those previously identified in literature [47] and the presence of non-uniform heating caused no newly identified flow patterns.
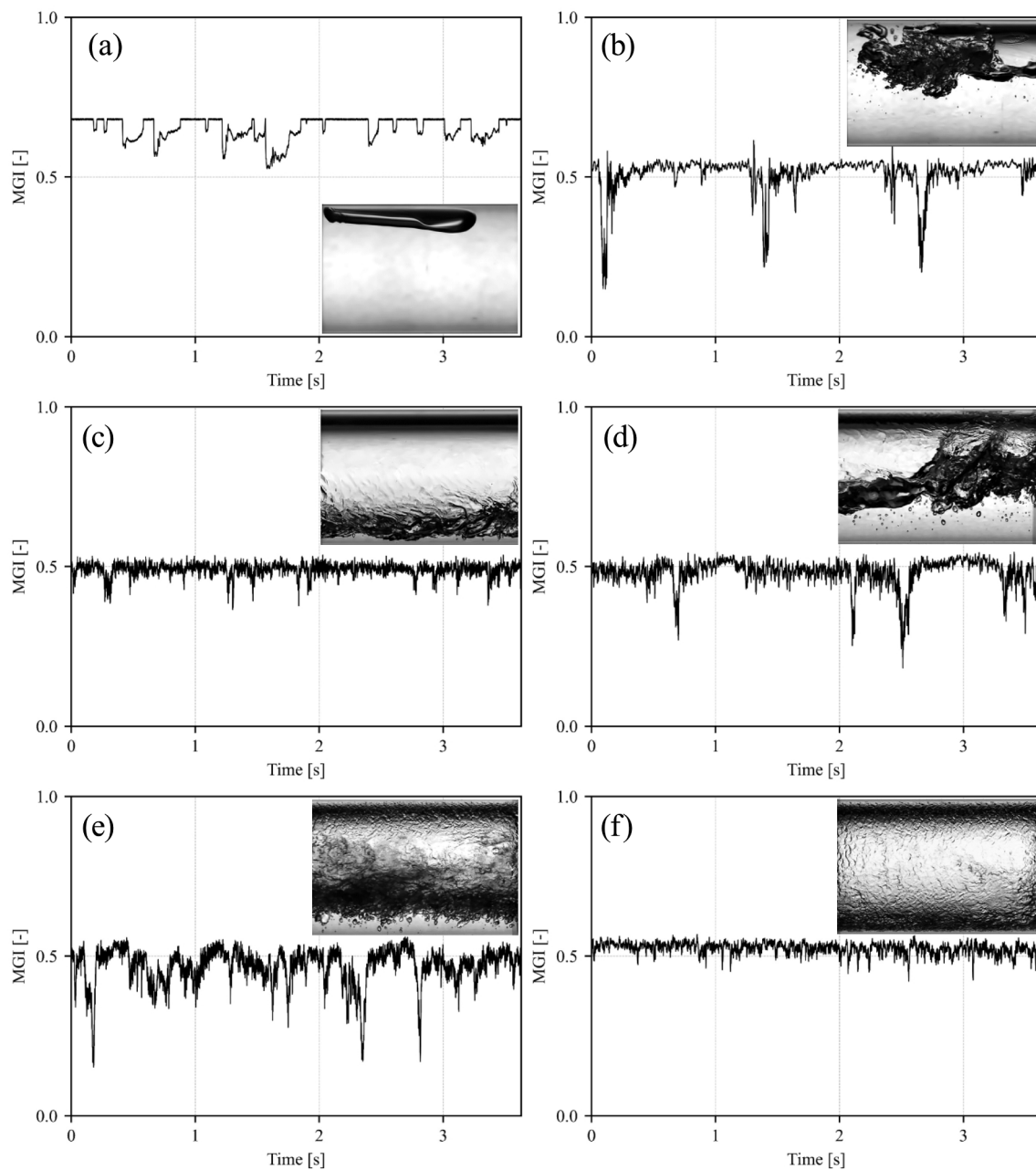
Fig. 10. Flow patterns and their MGI signals: (a) plug flow, (b) slug flow, (c) stratified-wavy flow, (d) slug/stratified-wavy flow, (e) intermittent flow, and (f) annular flow.

6.2. Flow pattern map

Fig. 11 displays the diabatic (test-section outlet) flow pattern data for all heat flux profiles, superimposed on the flow-pattern map of Wojtan, et al. [47] at the mean test condition ($T_{sat} = 40\,°C$, $G = 200\,kg/m^2s$). The map of Wojtan, et al. [47] is relatively invariant over the range of test conditions, allowing for a singular flow-pattern map to be used. As seen in Fig. 11, the flow patterns were identical for each set of x and G, implying the heat flux distribution had no observable influence on the transition between flow patterns. In contrast, Wang, et al. [41] noted semi-circumferential bottom heating to decrease the vapour quality of the intermittent-to-annular (I/A) transition boundary, which was attributed to flow instabilities caused by the locally increased heat flux. An opposing trend has been found in uniform heating investigations, where the vapour quality of the I/A transition increased with heat flux [58,59]. However, the mentioned studies were for smaller tube diameters. It is postulated that flow instabilities resulting from larger heat fluxes (at the same total heat rate) in non-uniform heating are negligible in comparison to the inertial forces for larger tube diameters, as employed in this study and used in PTC absorber tubes and waste-heat recovery systems. This can be seen by the flow pattern transition boundaries remaining unchanged given the large changes in local heat flux between the tested heating distributions.

The flow-pattern map of Wojtan, et al. [47] performs relatively well, predicting 71 % of the data correctly. The largest discrepancies occur at the I/A transition boundary, which is seen in Fig. 11 to be non-constant and dependent on mass flux. This can be explained by the flow becoming favourable to annular flow with the increase in mass flux, as the vapour velocity and liquid–vapour interfacial shear stress increase [57].

The I/A transition boundary is further investigated in Fig. 12 by analysing some I/A transition criteria from literature, as presented in Table 4. The constant boundary of Wojtan, et al. [47] performs poorly,
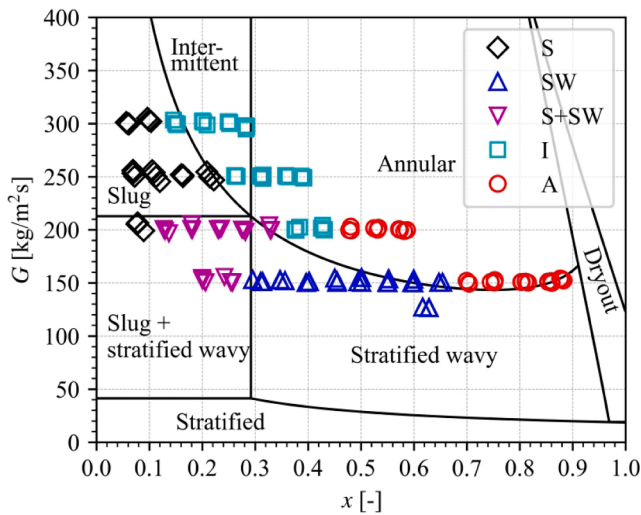
Fig. 11. Diabatic flow pattern data for all heat flux profiles, superimposed on the flow pattern map of Wojtan, et al. [47].
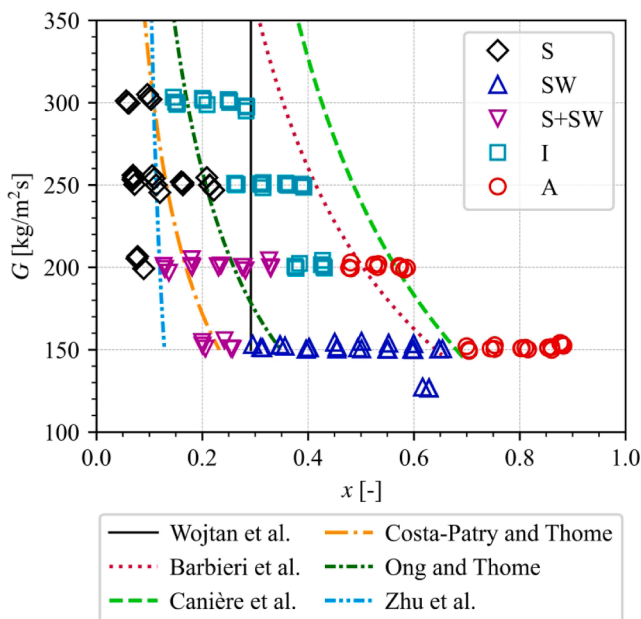

Fig. 12. Intermittent-to-annular transition boundary.

as it is unable to capture the dependency on mass flux. Barbieri, et al. [60] and Canière, et al. [61] account for the decrease in vapour quality with increases in mass flux, relying on a fundamental relation between the liquid Froude number (Fr_l) and Lockhart-Martinelli parameter (X_{tt}). Ong and Thome [62] proposed a different formulation, severely underpredicting the I/A transition. Costa-Patry and Thome [58] and Zhu, et al. [59] captured the dependency on heat flux via the boiling number (Bo). However, both correlations underpredict the I/A transition, as they were derived from tube diameters less than 3.04 mm. More data over the I/A transition boundary is required to make a conclusive statement. However, there is evidence to support the selection of Barbieri, et al. [60] I/A transition criteria, which improves the predictive accuracy of the flow-pattern map of Wojtan, et al. [47] to 86 %.

7. Uniform heat flux results

7.1. Average heat transfer coefficient

Besides the case of uniform heating (Case I) being important for larger tube diameters employed in industrial ORC evaporators – which is notably lacking in literature – the results will be used to make sense of the non-uniform heating cases in a later discussion. The average HTC's dependence on vapour quality and mass flux is displayed in Fig. 13. Generally, the HTC displayed a decreasing and then increasing trend with vapour quality and an increasing trend with mass flux.

The HTC for slug and slug/stratified-wavy flow decreased with an increase in vapour quality and a decrease in mass flux. This can be explained by the liquid slugs that intermittently wet the tube's upper circumference, creating a thin liquid film which subsequently recedes down the tube wall. As the vapour quality increases, the period of local dryout on the upper circumference increases by virtue of the reduction in liquid slugs, consequently decreasing the HTC. Increases in the mass flux enhances convective boiling and reduces viscous draining of the liquid film, while also increasing the frequency of liquid slugs, resulting in an improved heat transfer performance.

Notably, the HTC values approximately converged for $G = 150$ kg/m²s and 200 kg/m²s at $\bar{x} = 0.2$ to 0.3, which was attributed to the temporal-sparsity of liquid slugs and thus the reduced period of liquid film evaporation. Consequently, the contribution of convective boiling had diminished and thus the influence of mass flux.

The HTC for stratified-wavy flow displayed a slight decreasing trend followed by an increasing trend with vapour quality. Initially, there was a reduction in the height of the stratified phase interface, suppressing nucleate boiling. As vapour quality increased, a thin liquid film started to propagate up the tube wall, increasing convective boiling. Interestingly, a lower mass flux ($G = 125$ kg/m²s) in stratified-wavy flow indicated an enhanced HTC, which can be speculated to be due to the weakening of nucleate suppression at the reduced mass flux.

The HTC for intermittent and annular flow rapidly increased with vapour quality and mass flux. Increases to the vapour quality and mass flux strengthens the liquid–vapour interfacial shear stress and reduces the peripheral liquid film thickness. This decreases the liquid film's thermal resistance, leading to enhanced convective boiling.

7.2. Peripheral heat transfer coefficient

Fig. 14 displays the average lengthwise HTC values at different circumferential positions for various vapour quality and mass flux combinations, while the tube was in configuration (i) (see Fig. 2 (c)). Due to symmetry about the tube's vertical centre plane, corresponding heating element sectors have been grouped together. Fig. 14 (a) gives the local HTC for $n = 1, 2$ (at the bottom), corresponding to an angular heated sector position of $\theta \in \pm [0°; 45°]$, Fig. 14 (b) does the same for $n = 3, 8$ with $\theta \in \pm [45°; 90°]$, Fig. 14 (c) for $n = 4, 7$ with $\theta \in \pm [90°; 135°]$, and Fig. 14 (d) for $n = 5, 6$ (at the top) with $\theta \in \pm [135°; 180°]$. For easier reference, the peripheral regions are schematically indicated in the figures by black or grey arcs and correspond to the data plots with black and feint connector lines, respectively.

As can be seen in Fig. 14 (c) (as an example), the symmetric nature of the results is quite evident based on the close agreement between the data for $n = 7$ (black connectors) and $n = 4$ (feint connectors), except at $G = 300$ kg/m²s, which was an anomaly. Indicative uncertainty bars are included on the data for $G = 150$ kg/m²s from which larger uncertainties were associated with higher vapour quality conditions. As before, the prevailing flow patterns are indicated by the markers.

Indicative of nucleate boiling dominance, the HTC values in the lower half of the tube (Fig. 14 (a) and (b)) were found to be relatively independent of mass flux up to $x \approx 0.15$. For $x > 0.15$, the HTC in the lowest part of the tube (Fig. 14 (a)) increased with mass flux and vapour quality, which was caused by the resulting liquid film thinning and the

Table 4
Intermittent-annular transition criteria.

Author	Model	
Wojtan, et al. [47]		
	$$x_{\mathrm{I/A}} = \left\{ \left[0.34^{1/0.875} \left(\frac{\rho_{\mathrm{g}}}{\rho_{\mathrm{l}}} \right)^{-1/1.75} \left(\frac{\mu_{\mathrm{l}}}{\mu_{\mathrm{g}}} \right)^{-1/7} \right] + 1 \right\}^{-1}$$	(22)
	where ρ_{l} and ρ_{g} are the saturated liquid and vapour densities, while μ_{l} and μ_{g} are the saturated liquid and vapour dynamic viscosities, respectively.	
Barbieri, et al. [60]		
	$$Fr_{\mathrm{l}} = 3.75 X_{\mathrm{tt}}^{2.4}$$	(23)
Canière, et al. [61]		
	$$Fr_{\mathrm{l}} = (14.27 P_{\mathrm{A}} + 2.315) X_{\mathrm{tt}}^{\left(-0.618 P_{\mathrm{A}}^2 + 0.6975 P_{\mathrm{A}} + 2.504\right)}$$	(24)
	where $P_{\mathrm{A}} \in [0;1]$ is the probability of annular flow.	
Costa-Patry and Thome [58]		
	$$x_{\mathrm{I/A}} = 425 \left(\frac{\rho_{\mathrm{g}}}{\rho_{\mathrm{l}}} \right)^{0.1} \frac{Bo^{1.1}}{Co^{0.5}}$$	(25)
	where Co is the confinement number.	
Ong and Thome [62]		
	$$x_{\mathrm{I/A}} = 0.047 Co^{0.05} \left(\frac{\mu_{\mathrm{g}}}{\mu_{\mathrm{l}}} \right)^{0.7} \left(\frac{\rho_{\mathrm{g}}}{\rho_{\mathrm{l}}} \right)^{0.6} Re_{\mathrm{go}}^{0.8} We_{\mathrm{lo}}^{-0.91}$$	(26)
	where Re_{go} is the gas-only Reynolds number and We_{lo} is the liquid-only Weber number.	
Zhu, et al. [59]		
	$$x_{\mathrm{I/A}} = 0.03388 Co^{0.2829} \left(\frac{\mu_{\mathrm{g}}}{\mu_{\mathrm{l}}} \right)^{0.5371} \left(\frac{\rho_{\mathrm{g}}}{\rho_{\mathrm{l}}} \right)^{0.6786} Re_{\mathrm{go}}^{0.8094} We_{\mathrm{lo}}^{-0.4297} Bo^{0.1984}$$	(27)

enhancement of convective boiling. In contrast, the HTC higher up the tube wall (Fig. 14 (b)) was relatively unaffected by mass flux, and therefore remained largely dominated by nucleate boiling.

The HTC magnitudes of the upper half of the tube (Fig. 14 (c) and (d)) were significantly affected by both the mass flux and vapour quality, emphasising the dominance of convective boiling. The HTC initially decreased with vapour quality, after which there was a rapidly increasing region. The onset of the increase was in good agreement with the transition to intermittent and annular flow, as can be seen from the flow pattern markers. The liquid slugs associated with slug and slug/stratified-wavy flow formed a thin liquid film on the tube's upper

Fig. 13. Uniform heat flux average heat transfer coefficients.

circumference, which has been found to reduce the suppression of bubble nucleation (via a slower moving liquid film) and enhance convective boiling (via thin film evaporation) [63]. Consequently, the HTC at low vapour qualities increase with mass flux, while suffering from the reduction in liquid slug frequency with increases in vapour quality. With the transition to intermittent and annular flow, the convective boiling mechanism was enhanced with vapour quality and mass flux.

It is evident that under uniform heat flux conditions the local HTC varies significantly around the tube's circumference, emphasising the importance of the phase asymmetry (the tendency of the liquid phase to accumulate at the bottom of the tube due to gravity) in larger tube diameters. At lower mass fluxes and vapour qualities, the lower circumference has a superior heat transfer capacity as the thicker liquid film is advantageous to nucleate boiling. However, for higher mass fluxes and vapour qualities, the thinner liquid film at the tube's upper circumference is advantageous to convective boiling heat transfer, outperforming the thicker liquid film at the lower circumference that is less favourable to convective mechanisms.

7.3. Predictive models from literature

Fig. 15 compares the obtained HTC values at the uniform heat flux to six well-known correlations from literature. Table 5 gives a summary of the mean absolute error (MAE), mean relative error (MRE), and the percentage of data captured within ± 30 % error. The Wojtan, et al. [40] flow-pattern based correlation is the most accurate at a MAE of 16.7 % and captures 88.1 % of the data within ± 30 %. Shah, et al. [64] provides a simpler model with the next-best MAE of 18.8 %. Kandlikar [65] performs similarly as well but captures 85.7 % of the data points within ± 30 %. Kandlikar's [65] correlation introduces a fluid-dependent parameter that was taken to be 1.3 as proposed by Moran, et al. [66]. An optimisation on the current data set gave a similar value of 1.1 to
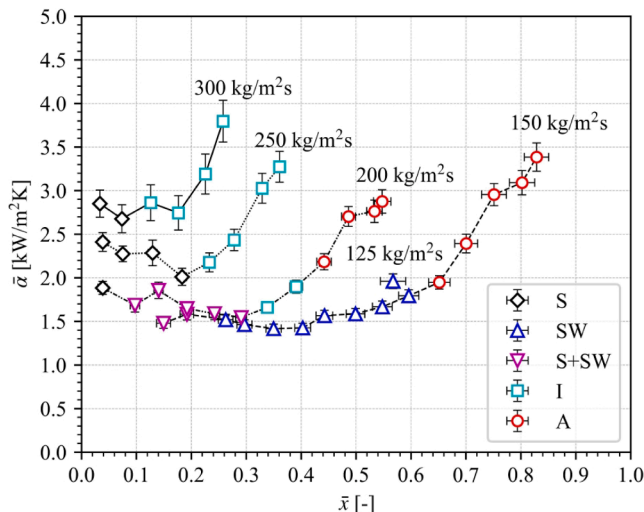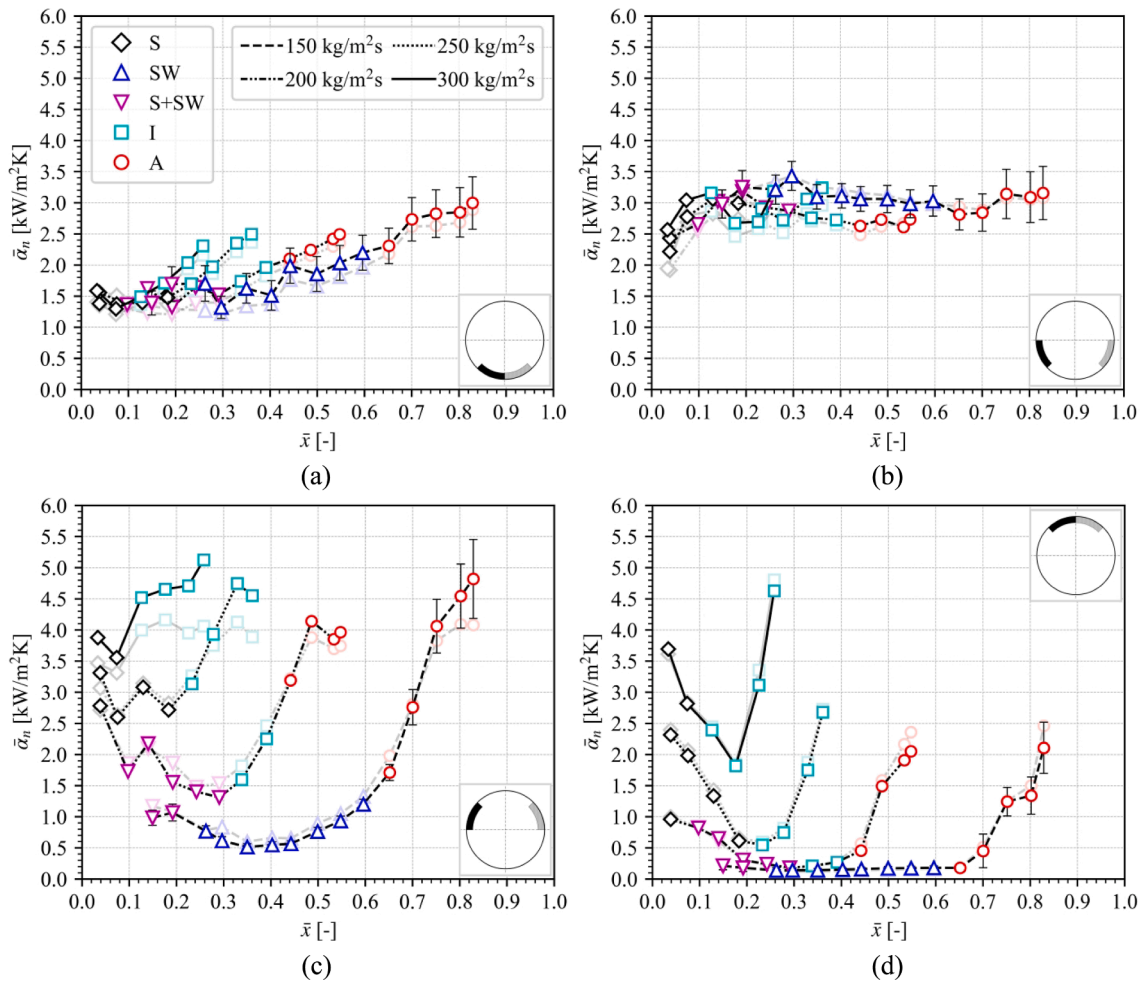
Fig. 14. Average lengthwise heat transfer coefficients for each mass flux at (a) $\theta \in \pm [0°; 45°]$, (b) $\theta \in \pm [45°; 90°]$, (c) $\theta \in \pm [90°; 135°]$, and (d) $\theta \in \pm [135°; 180°]$.

gain marginal improvements (resulting in a MAE of 19.2 %). The correlation of Fang, et al. [37] was also evaluated and displays a remarkable MAE of only 2.8 %. However, the model requires detailed knowledge of the local wetted-wall heat fluxes and temperatures and is therefore not comparable. From the experimental data in Fig. 15, it can be noted that all the evaluated correlations generally overpredict the HTC for stratified-wavy and slug/stratified-wavy flow (nucleate boiling dominant flow), while underpredicting the HTC for slug, intermittent, and annular flow (convective boiling dominant flow).

8. Non-uniform heat flux results

8.1. Average heat transfer coefficient

Fig. 16 supplies a comparison of the average HTC of the various heat flux profiles for different mass fluxes, with the symbols provided in Fig. 16 (b). The experimentally observed flow pattern transition lines (identified in Fig. 11) are also plotted for reference. It is evident the heat flux distribution (for the same total heat load) had a significant influence on the average HTC. PTC profile heating (Case V) indicated in red produced the highest HTC, only to be surpassed by uniform heating (Case I) in latter regions of intermittent and annular flow, as seen for instance in Fig. 16 (a) (for $G = 150$ kg/m^{2}s, and $x = 0.8$). Top half heating (Case III) shown in purple, performed the worst and resulted in elevated test-section temperatures and was prone to local dryout. To protect the test section, the number of data points produced for this heating profile were reduced.

After the PTC heating profile (Case V), bottom half heating (Case II), given in blue, produced the next best thermal performance at low mass fluxes and vapour qualities (Fig. 16 (a) to (c)). As in PTC profile heating, the HTC for bottom half heating was not strongly influenced by vapour quality. This is because the lower circumference, where the bulk of the heating was concentrated, was always covered with a thick liquid film in which bubble nucleation and departure were enhanced with increases in local heat flux. Whereas the tube's upper circumference for these low mass fluxes and vapour qualities was dry, or partially dry, and had a weak affinity to the local heat flux. Thus, uniform (Case I), top half (Case III), and side half (Case IV) heating did not perform as efficiently.

In contrast, as the mass flux and vapour quality increased, heating profiles that had a significant heating contribution at the upper regions of the tube (Cases I, III, and IV) were much more likely to exhibit an improvement in the HTC. This is because of the relatively thinner liquid layer that developed on the tube's upper circumference at these flow conditions, which is dominated by convective boiling. Convective boiling heat transfer is improved with the increase in local flow velocities and the reduction in the liquid film thickness, which is caused either by a higher applied mass flux or induced by a higher vapour quality. However, for these higher mass fluxes and vapour qualities, the nucleate boiling dominance of the lower circumference is suppressed via liquid film thinning and increased liquid turbulence, weakening the HTC for bottom half (Case II) and PTC profile (Case V) heating.

Slug flow provided an interesting phenomenon where nucleate boiling dominated the lower circumference due to a thick liquid film, while a thin, slower-moving liquid film on the upper circumference from

passing liquid slugs was largely dominated by convective boiling. As a result, the HTC magnitudes were generally similar between heat flux profiles.

The superiority of uniform heating (Case I) for highly convective boiling flow conditions can be explained by the approximate alignment of the heat flux and HTC distributions. Convective boiling during intermittent and annular flow is dominated by thin liquid film evaporation of the liquid annulus, which is mostly inert to heat flux. It follows that uniformly distributing the heat load best aligns with the near uniform HTC distribution, being optimal for the average heat transfer performance. The increase in vapour quality tends to improve the circumferential uniformity of the liquid film and thus the HTC magnitudes, further improving the heat-flux-to-HTC alignment. Similarly, Dirker, et al. [42] found uniform heating in annular flow to be superior to several non-uniformly distributed heat loads.

8.2. Effect of mass flux

Fig. 17 displays the effect of the mass flux on the average HTC for each heat flux profile. Bottom half (Case II) and PTC profile (Case V) heating, shown in Fig. 17 (a) and Fig. 17 (d) respectively, were approximately independent of mass flux, indicative of nucleate boiling dominance. Similar observations have been made for CO_2 flow boiling and has been explained by the dominance of nucleate boiling [70]. Top half (Case III) and side half (Case IV) heating, shown in Fig. 17 (b) and Fig. 17 (c) respectively, displayed an increasing trend with mass flux across all vapour qualities, indicating the presence of convective boiling mechanisms.

This provides useful insight, as PTC and other NUHF technologies can operate at lower mass fluxes provided the heat flux is distributed towards the lower circumference of the tube – towards the liquid phase accumulation at the lower circumference – which implies reduced pump power and associated costs.

8.3. Relative heat transfer performance

The relative heat transfer performance of the non-uniform cases to the uniform case are presented in Fig. 18 by considering the ratio of average HTC ($\bar{\alpha}/\bar{\alpha}_{\text{uniform}}$).

Table 5
Predictive accuracy of heat transfer coefficient correlations.

Correlations	MAE[1] [%]	MRE[2] [%]	Data within $\pm$ 30 % error [%]
Shah [64]	18.8	− 7.1	69.0
Kandlikar [65]	19.6	+ 3.8	85.7
Wojtan, et al. [40]	16.7	− 2.4	88.1
Gungor and Winterton [67]	20.7	+ 0.6	81.0
Saitoh, et al. [68]	20.4	− 16.9	59.5
Liu and Winterton [69]	21.6	− 1.2	78.6

[1]MAE $= \dfrac{1}{N}\sum_{1}^{N}\dfrac{\left|\bar{\alpha}_{\text{cal}} - \bar{\alpha}_{\text{exp}}\right|}{\bar{\alpha}_{\text{exp}}} \bullet 100$, [2]MRE $= \dfrac{1}{N}\sum_{1}^{N}\dfrac{\bar{\alpha}_{\text{cal}} - \bar{\alpha}_{\text{exp}}}{\bar{\alpha}_{\text{exp}}} \bullet 100$.

Bottom half (Case II) and PTC profile (Case V) heating, shown in Fig. 18 (a) and Fig. 18 (d), exhibited the largest scatter in relative performance, ranging between a 40 % and 18 % reduction to an 80 % and 144 % enhancement, respectively. The relative performance initially increased with vapour quality, as the phase asymmetry developed (initial vapour bubbles accumulated on the upper circumference) and the rate of heat transfer for uniform heating reduced. After reaching a maximum, the relative performance decreased with further increases to vapour quality, as uniform heating harnessed the liquid film evaporation of the upper circumference, while the nucleate boiling dominance of bottom half (Case II) and PTC profile (Case V) heating remained relatively unaffected. The relative performance reduced with increases in mass flux. Increases to the mass flux accelerated the transition to, and increased the magnitude of, convective boiling for uniform heating (Case I), as compared with the near constant nucleate boiling performance of bottom half (Case II) and PTC profile (Case V) heating. The upshift in relative performance for PTC profile heating (Case V) over semi-circumferential bottom half heating (Case II) was a result of the larger local heat flux and strengthened nucleate boiling mechanism.

Top half heating (Case III), shown in Fig. 18 (b), only recorded data points once a thin liquid film developed on the upper circumference, which was convective boiling dominant. Consequently, the relative performance remained at approximately a 40 % reduction, as the HTC
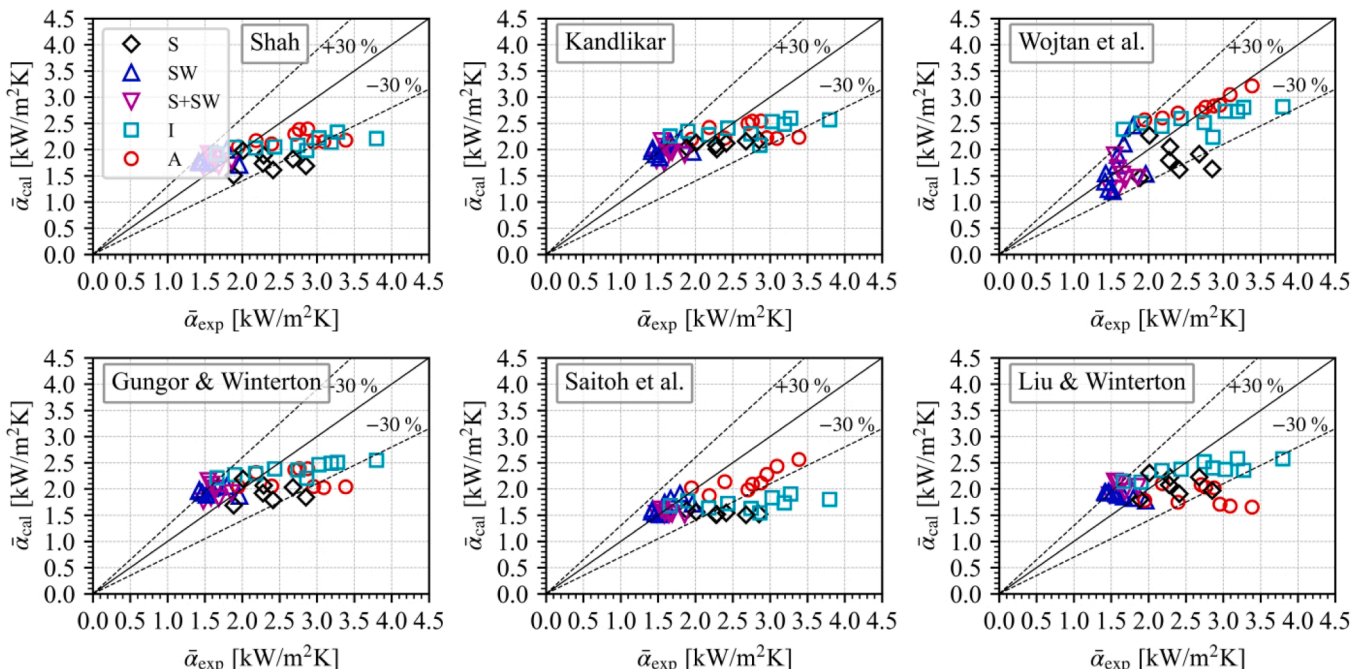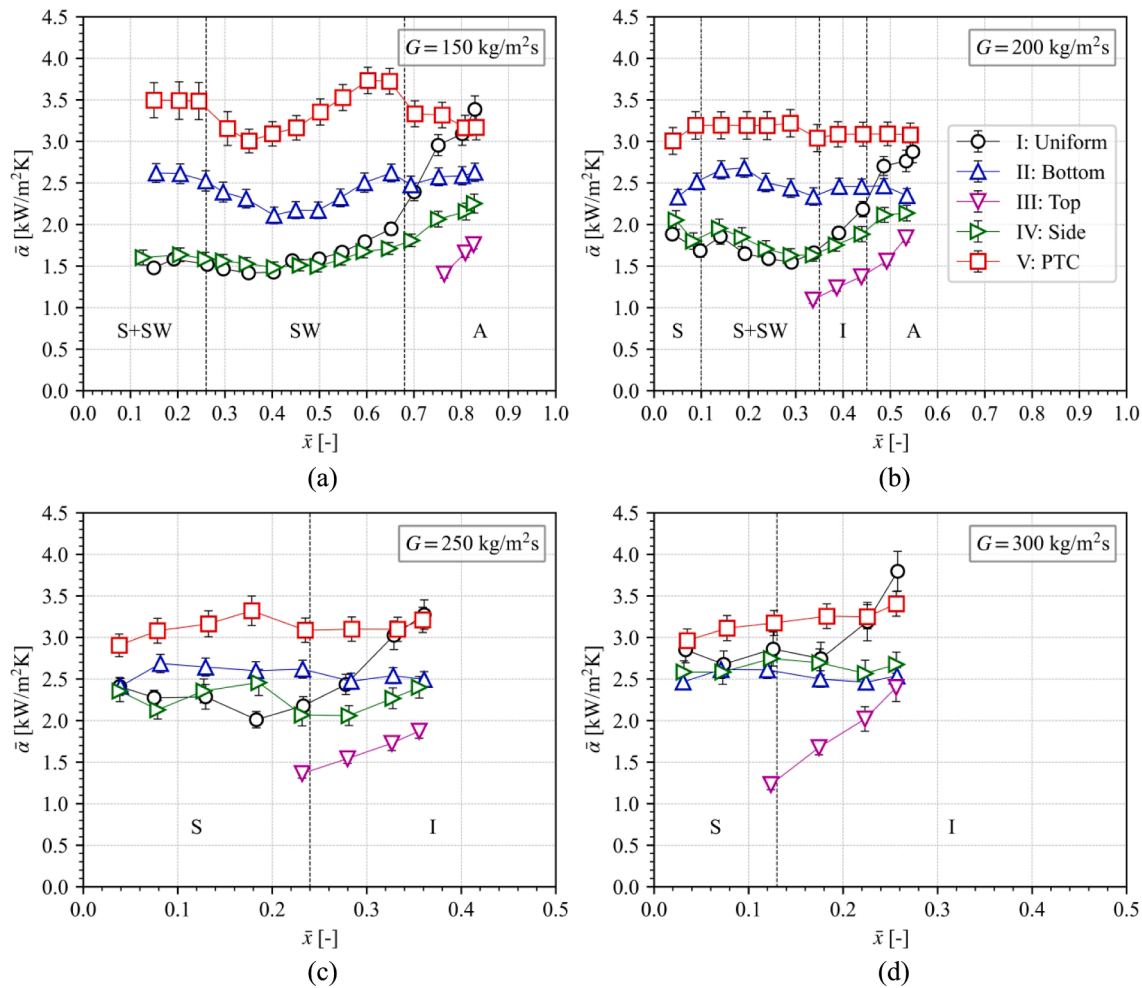

Fig. 15. Comparison of the calculated versus experimental heat transfer coefficients for the uniform heat flux.

Fig. 16. Comparison of the average heat transfer coefficients for all heat flux profiles at (a) $G = 150$ kg/m²s, (b) $G = 200$ kg/m²s, (c) $G = 250$ kg/m²s, and (d) $G = 300$ kg/m²s.

values were unaffected by the increased heat flux and suffered from the reduction in heat transfer surface area of top half heating.

Side half heating (Case IV), shown in Fig. 18 (c), had a reduced scatter in relative performance, ranging between a 35 % reduction to a 25 % enhancement in performance. Since both side half (Case IV) and uniform (Case I) heating distributed the heat load uniformly across the phase asymmetry, similar heat transfer mechanisms were activated and resulted in quantitively similar trends with mass flux and vapour quality. Only at highly convective boiling flow did side half heating (Case IV) suffer in relative performance by virtue of the reduced heat transfer area and convective boiling's inert response to heat flux.

It is clear the average HTC for semi-circumferential bottom half heating (Case II) varies significantly from PTC profile heating (Case V), implying a semi-circumferential heat flux profile is not an accurate way of representing the thermal condition in PTC absorber tubes. Therefore, the PTC heating profile should not be simplified to a semi-circumferential bottom half heating profile when modelling PTC tubes, as this can lead to an inaccurate model.

9. Local heat transfer coefficient

### 9.1. Local heat transfer coefficient response to heat flux

Fig. 19 displays the local HTC values versus the local heat flux at different peripheral locations around the tube in terms of the angular position of the heating element sector: (a) $\theta \in \pm [0°; 45°]$, (b) $\theta \in \pm [45°; 90°]$, (c) $\theta \in \pm [90°; 135°]$, and (d) $\theta \in \pm [135°; 180°]$. As before,

symmetry was used to group relevant sectors. The Cooper [39] pool boiling correlation (α_{nb}) is superimposed for discussion purposes.

It should be noted that in this study the lower portion of the tube was constantly wetted by a liquid layer due to the horizontal arrangement and gravitational force. At the lowest tube region with $\theta \in \pm [0°; 45°]$ (Fig. 19 (a)), a HTC lower bound corresponding to approximately 60 % of the Cooper [39] pool boiling prediction ($0.6\alpha_{nb}$) was found to exist, while the HTC lower bound for slightly higher up the tube wall at $\theta \in \pm [45°; 90°]$ (Fig. 19 (b)) required no correction (α_{nb}). By deduction, the suppression of nucleate boiling increased towards the bottom of the tube for the consistently wetted lower circumference. Moran, et al. [66] noted the interfacial waves in stratified-wavy flow induces secondary flow, which diminishes toward the bottom of the tube. The secondary flow removes hot fluid at the tube wall and replaces it with cooler fluid, increasing the temperature gradient between the tube wall and fluid [66]. Therefore, the interfacial waves in the nucleate boiling dominant flow patterns induced secondary flow over the region of $\theta \in \pm [45°; 90°]$ and made for the effective superheat to be equivalent to that of pure nucleate boiling ($T_w - T_{sat}$), resulting in no nucleate suppression. Whereas the secondary flow had mostly dissipated before the bottom of the tube, that being the lowest region of the tube at $\theta \in \pm [0°; 45°]$, resulting in a reduced effective wall superheat and thus the suppression of bubble nucleation.

The tube's upper circumference (Fig. 19 (c) and (d)) followed considerably different trends to the lower circumference. The tube's apex at $\theta \in \pm [135°; 180°]$ was either dry or subjected to thin film evaporation. Consequently, the local HTC did not have a nucleate
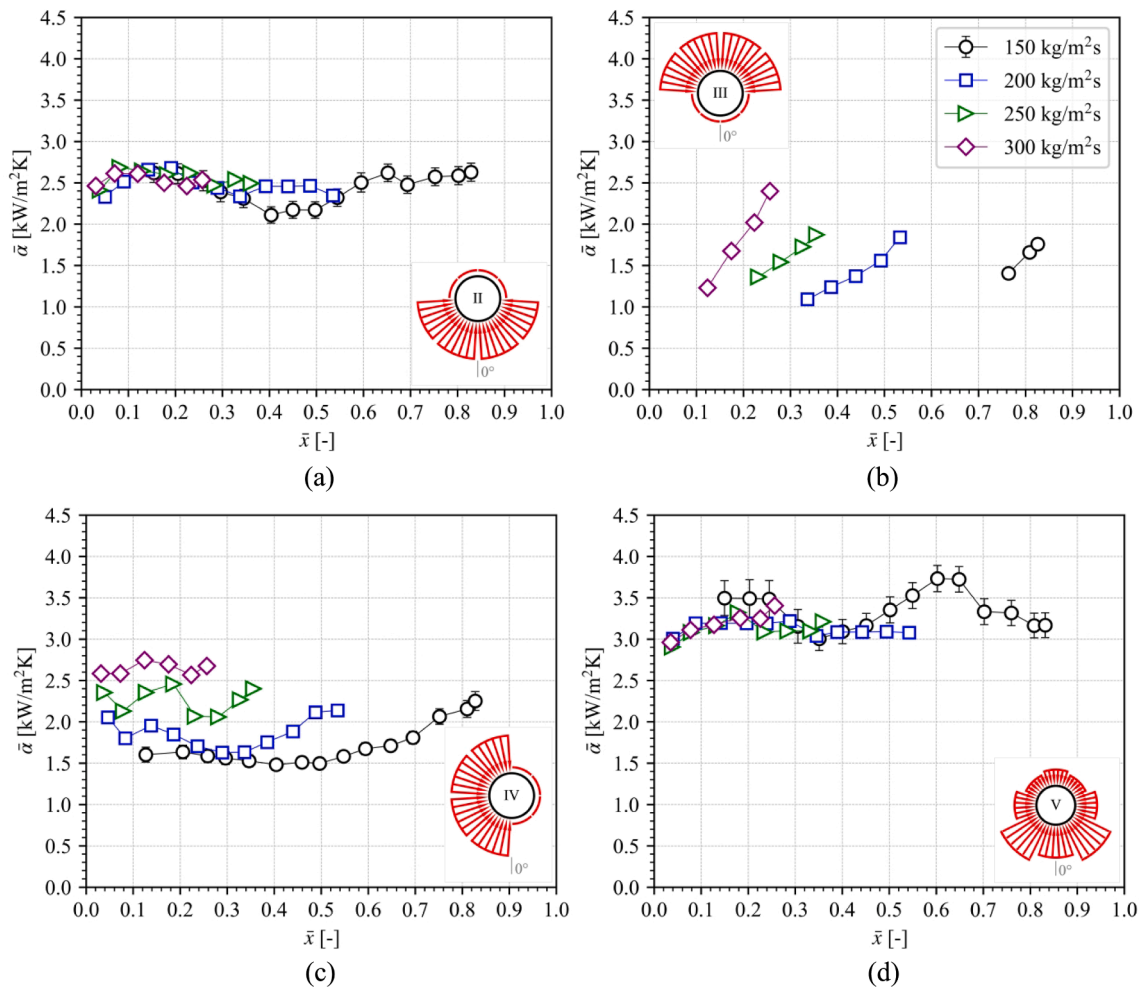
Fig. 17. Effect of mass flux of the average heat transfer coefficient for different heat flux profiles: (a) bottom half, (b) top half, (c) side half, and (d) PTC profile heating. Only uncertainty bars for $G = 150$ kg/m^{2}s are displayed.
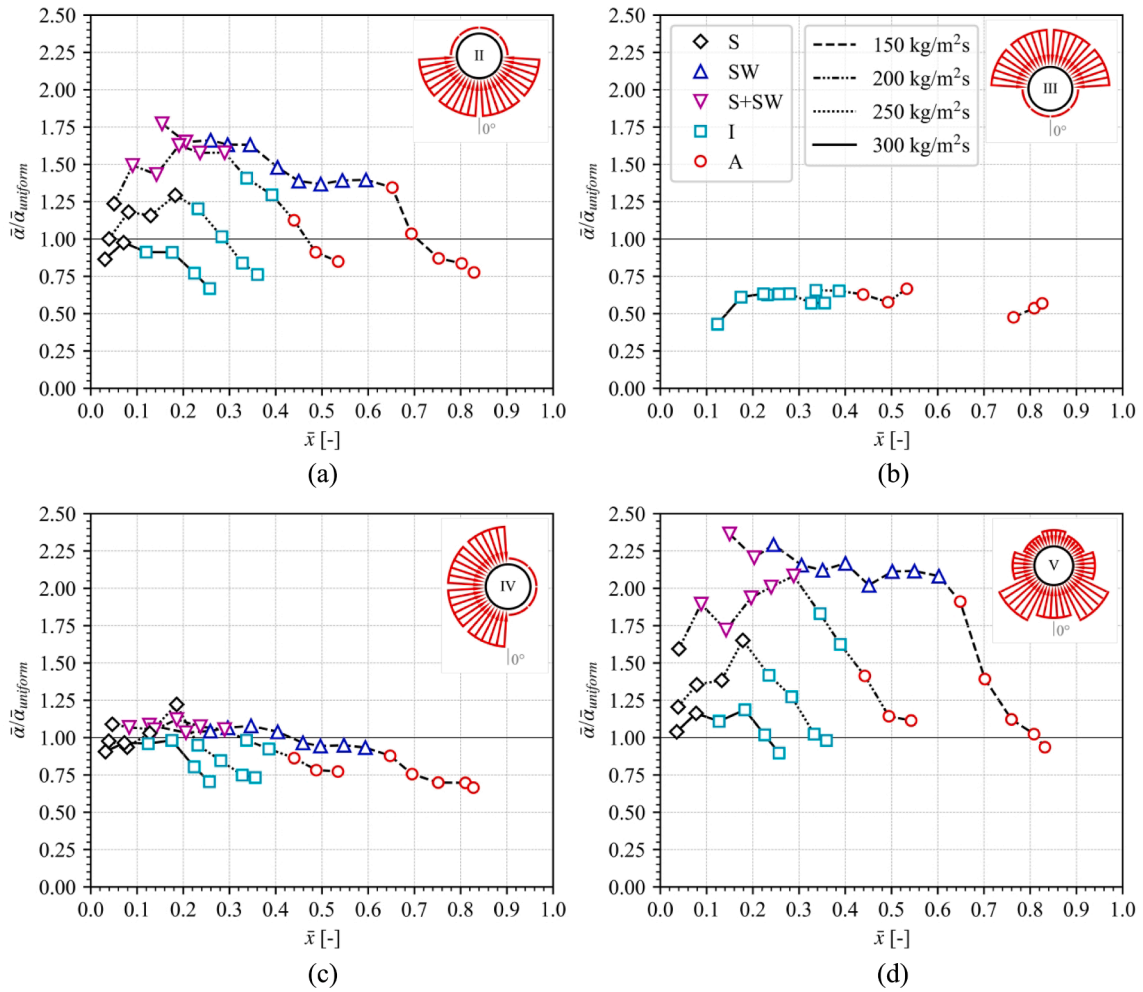
Fig. 18. Relative heat transfer performance of the non-uniform cases to uniform case for (a) bottom half, (b) top half, (c) side half, and (d) PTC profile heating.
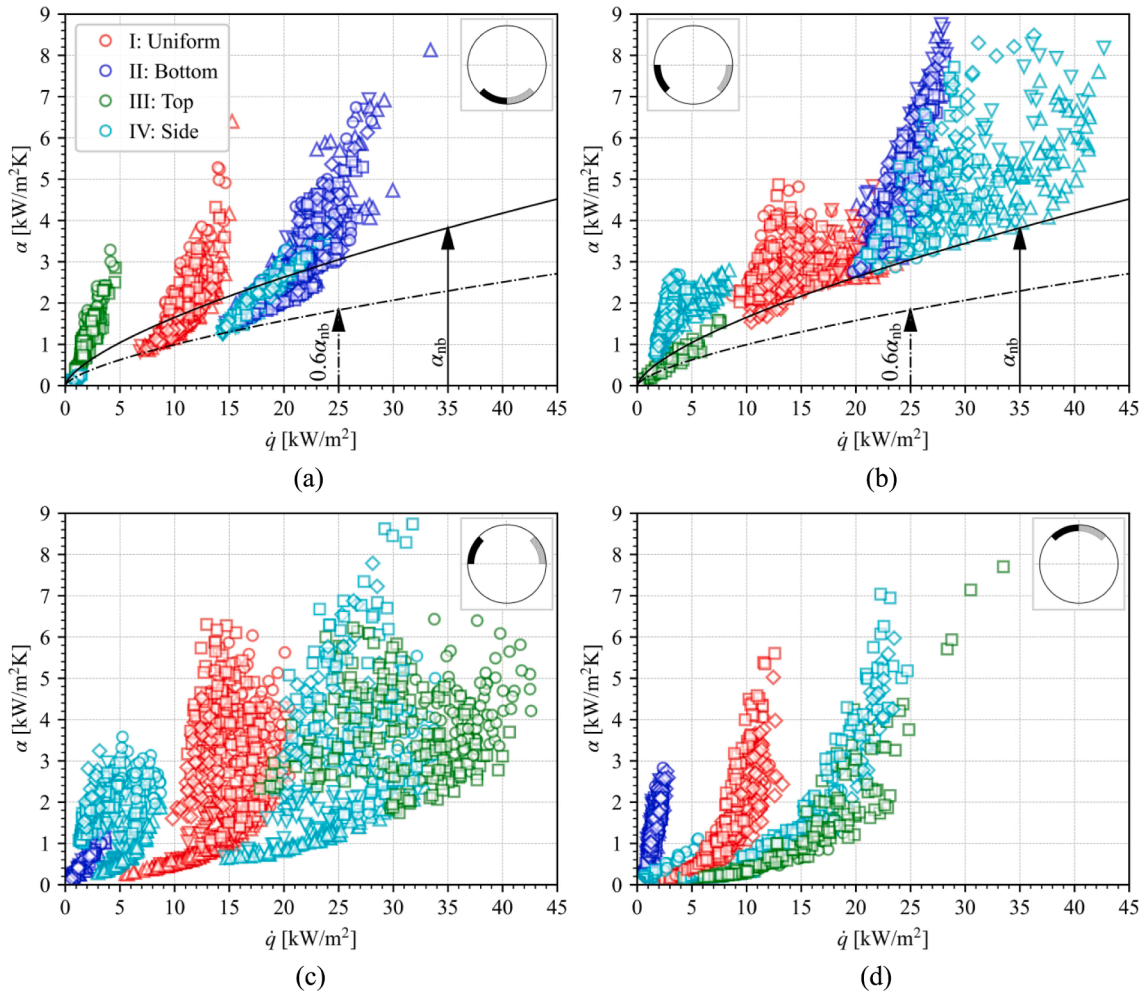
Fig. 19. Local heat transfer coefficients versus local heat flux at peripheral locations (a) $\theta \in \pm [0°; 45°]$, (b) $\theta \in \pm [45°; 90°]$, (c) $\theta \in \pm [90°; 135°]$, and (d) $\theta \in \pm [135°; 180°]$.
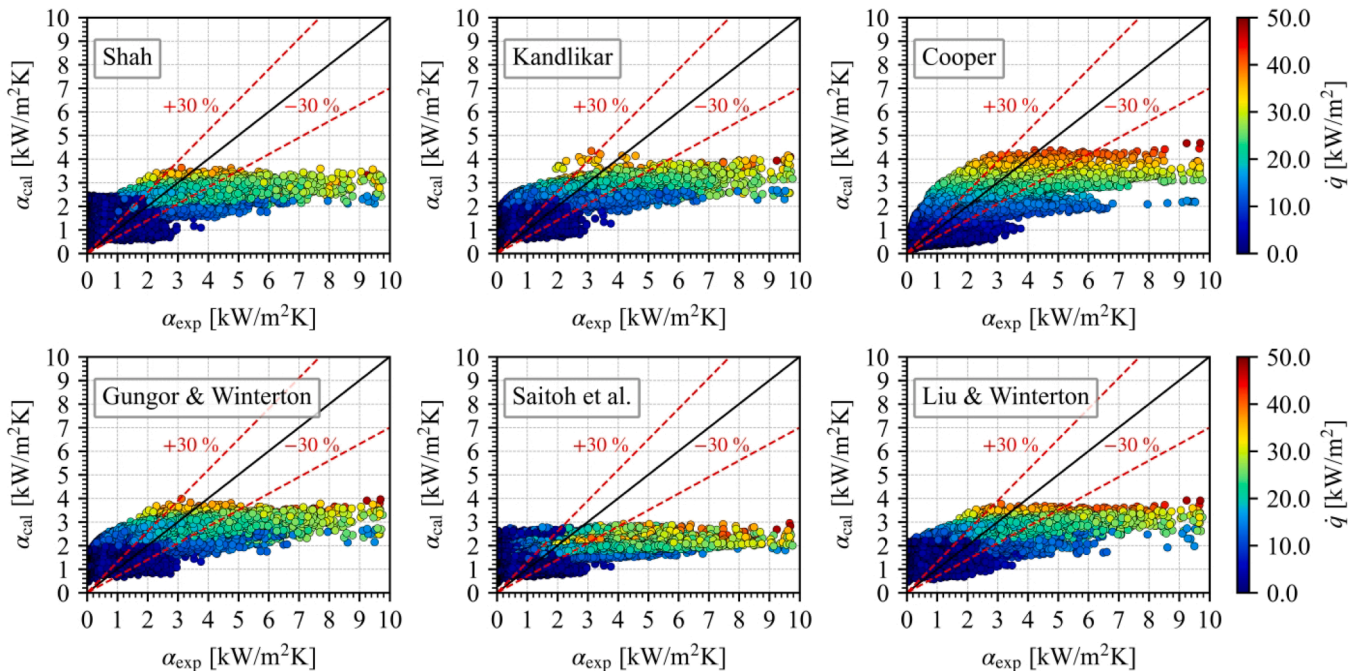

Fig. 20. Comparison of the calculated versus experimental heat transfer coefficients at the local level, shaded in terms of local heat flux.
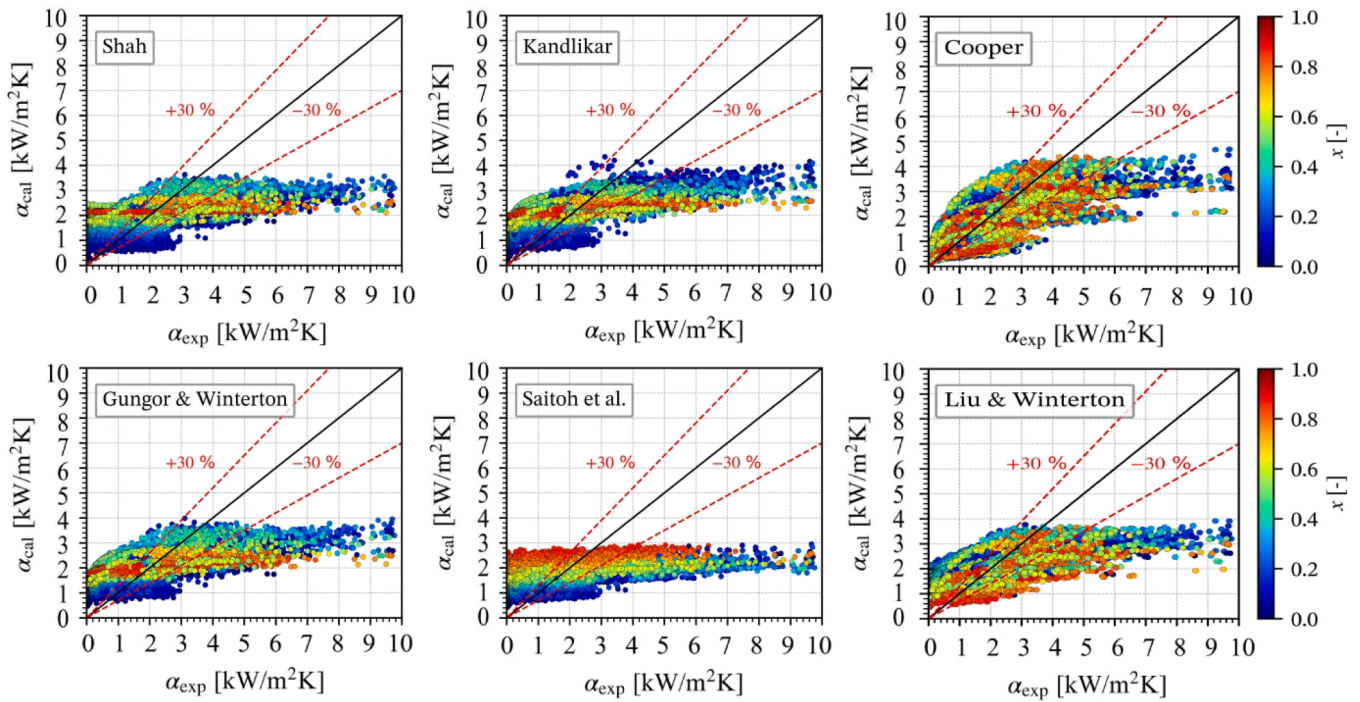
Fig. 21. Calculated versus experimental heat transfer coefficients at the local level, shaded in terms of local vapour quality.

boiling lower bound, and convective heat transfer dominated. Slightly lower down the tube wall at $\theta \in \pm [90°; 135°]$ (Fig. 19 (c)) similar behaviour was obtained, however, with a larger scatter in respects to heat flux as mechanisms of nucleate boiling were superimposed, depending on the flow pattern.

9.2. Predictive methods from literature at the local level

Fig. 20 displays the predicted versus experimental HTC magnitudes at each local surface (m, n). The heat flux employed in the correlations was the local wetted-wall heat flux, where the magnitude is indicated via the data point colour. As clearly identified in Fig. 20, existing correlations perform poorly at the local level, which is to be expected as they were derived and purposed for the average HTC. Consequently, the local HTC values at low heat flux regions are severely overpredicted by most of the included correlations, and the rate of increase in the local HTC (when compared to the experimental values) is underpredicted. Compared to the other correlations, the pool boiling correlation of Cooper [39] has a stronger dependency on the local heat flux and, thus, can more suitable capture the local HTC increasing trend with local heat flux.

While not displayed in Fig. 20, the correlation of Fang, et al. [37] was evaluated and performed extremely well with a MAE of 2.5 %. However, the application of the correlation remains limited as it requires detailed knowledge of the wetted-wall temperatures, which in this data set was known, and explains the good agreement.

Similar to Fig. 20, Fig. 21 presents the same comparison between the calculated local HTC and experimentally obtained local HTC values, but now shaded in terms of the local vapour quality instead of the local heat flux. From the figure it is clear that no direct dependence can be observed between the prediction accuracies on the local vapour quality. Instead, for all vapour qualities each correlation exhibits a wide range of under- to over-prediction of the local HTC.

This alludes to the fact that, by nature, the existing average HTC correlations are not suitable for local implementation and that further investigation is required to better understand and predict the local flow boiling heat transfer mechanism, particularly in cases with varying liquid layer thickness and heat flux intensities around the circumference of a tube.

10. Conclusion

In this investigation experimental data was gathered to aid in the fundamental understanding of the thermohydraulic characteristics of flow boiling subjected to non-uniform heating, This is of particular interest for direct steam/vapour generation in parabolic trough collectors. Saturated flow boiling of R245fa in a 17.12 mm diameter horizontal stainless-steel tube was studied at a variety of circumferential heat flux profiles. Based on the results it was found that:

- The applied heat flux profile influenced the local and average heat transfer coefficients.
- Irrespective of the applied heat flux profile, the obtained flow patterns agreed with those previously identified in literature and their transition boundaries were inert to the heat flux distribution. The flow-pattern map of Wojtan, et al. [47] describes the experimental data relatively well, while the proposal of Barbieri, et al. [60] better captures the intermittent-to-annular transition boundary.
- The uniformly applied heat flux resolved significant circumferential non-uniformities in the heat transfer coefficients, where the local heat transfer mechanisms were intrinsically linked to the accompanying flow pattern.
- The average heat transfer coefficient for the uniform heat flux was most accurately described by the flow-pattern based correlation of Wojtan, et al. [40].
- The parabolic trough collector heating profile had the highest heat transfer coefficient for most flow conditions, with a maximum relative performance to uniform heating of a 144 % enhancement, followed by bottom heating at an 80 % maximum enhancement.
- Uniform heating was superior at highly convective boiling flow conditions by approximately 40 % to semi-circumferential heating.
- Lower circumference positions were dominated by nucleate boiling mechanisms while the upper circumference positions were dominated by convective mechanisms.

Further research is required on predictive methods for resolving the local heat transfer coefficients.

CRediT authorship contribution statement

Declaration of Competing Interest

The authors declare that they have no known competing financial interests or personal relationships that could have appeared to influence the work reported in this paper.

Data availability

Data will be made available on request.

Acknowledgements

References

[1] J. Sun, Q. Liu, H. Hong, Numerical study of parabolic-trough direct steam generation loop in recirculation mode: Characteristics, performance and general operation strategy, Energ. Conver. Manage. 96 (2015) 287–302.

[2] E. Kabir, P. Kumar, S. Kumar, A.A. Adelodun, K.-H. Kim, Solar energy: Potential and future prospects, Renew. Sustain. Energy Rev. 82 (2018) 894–900.

[3] S.A. Kalogirou, Chapter 3 - Solar Energy Collectors, in: S.A. Kalogirou (ed.) Solar Energy Engineering (Second Edition), Academic Press, Boston, 2014, pp. 125-220.

[4] M.T. Islam, N. Huda, A.B. Abdullah, R. Saidur, A comprehensive review of state-of-the-art concentrating solar power (CSP) technologies: Current status and research trends, Renew. Sustain. Energy Rev. 91 (2018) 987–1018.

[5] A. Fernández-García, E. Zarza, L. Valenzuela, M. Pérez, Parabolic-trough solar collectors and their applications, Renew. Sustain. Energy Rev. 14 (2010) 1695–1721.

[6] X.D. Wang, L. Zhao, J.L. Wang, Experimental investigation on the low-temperature solar Rankine cycle system using R245fa, Energ. Conver. Manage. 52 (2011) 946–952.

[7] A. Jahan Zeb, J. Yu, F. Yongqiang, A. Muhammad, Q. Wang, P. Gang, Performance Assessment of Direct Vapor Generation Solar Organic Rankine Cycle System Coupled with Heat Storage, in, Vol. 14, 2022, pp. 15296.

[8] G. Xu, G. Song, X. Zhu, W. Gao, H. Li, Y. Quan, Performance evaluation of a direct vapor generation supercritical ORC system driven by linear Fresnel reflector solar concentrator, Appl. Therm. Eng. 80 (2015) 196–204.

[9] H. Chen, D.Y. Goswami, E.K. Stefanakos, A review of thermodynamic cycles and working fluids for the conversion of low-grade heat, Renew. Sustain. Energy Rev. 14 (2010) 3059–3067.

[10] E. Galloni, G. Fontana, S. Staccone, Design and experimental analysis of a mini ORC (organic Rankine cycle) power plant based on R245fa working fluid, Energy 90 (2015) 768–775.

[11] C.N. Markides, Low-concentration solar-power systems based on organic rankine cycles for distributed-scale applications: Overview and further developments, Front. Energy Res. 3 (2015).

[12] D. Wang, X. Ling, H. Peng, Performance analysis of double organic Rankine cycle for discontinuous low temperature waste heat recovery, Appl. Therm. Eng. 48 (2012) 63–71.

[13] S.M. Jeter, Analytical determination of the optical performance of practical parabolic trough collectors from design data, Sol. Energy 39 (1987) 11–21.

[14] S.M. Jeter, Calculation of the concentrated flux density distribution in parabolic trough collectors by a semifinite formulation, Sol. Energy 37 (1986) 335–345.

[15] Y. Qiu, M.-J. Li, Y.-L. He, W.-Q. Tao, Thermal performance analysis of a parabolic trough solar collector using supercritical CO2 as heat transfer fluid under non-uniform solar flux, Appl. Therm. Eng. 115 (2017) 1255–1265.

[16] Z.D. Cheng, Y.L. He, J. Xiao, Y.B. Tao, R.J. Xu, Three-dimensional numerical study of heat transfer characteristics in the receiver tube of parabolic trough solar collector, Int. Commun. Heat Mass Transfer 37 (2010) 782–787.

[17] J. Lu, Q. Yuan, J. Ding, W. Wang, J. Liang, Experimental studies on nonuniform heat transfer and deformation performances for trough solar receiver, Appl. Therm. Eng. 109 (2016) 497–506.

[18] V. Flores, R. Almanza, Behavior of the compound wall copper–steel receiver with stratified two-phase flow regimen in transient states when solar irradiance is arriving on one side of receiver, Sol. Energy 76 (2004) 195–198.

[19] Y. Wang, Q. Liu, J. Lei, H. Jin, A three-dimensional simulation of a parabolic trough solar collector system using molten salt as heat transfer fluid, Appl. Therm. Eng. 70 (2014) 462–476.

[20] N. Abed, I. Afgan, A. Cioncolini, H. Iacovides, A. Nasser, T. Mekhail, Thermal performance evaluation of various nanofluids with non-uniform heating for parabolic trough collectors, Case Stud. Therm. Eng. 22 (2020), 100769.

[21] Z. Huang, Z.-Y. Li, W.-Q. Tao, Numerical study on combined natural and forced convection in the fully-developed turbulent region for a horizontal circular tube heated by non-uniform heat flux, Applied Energy: Part 2, 185 (2017) 2194-2208.

[22] I.F. Okafor, J. Dirker, J.P. Meyer, Influence of non-uniform heat flux distributions on the secondary flow, convective heat transfer and friction factors for a parabolic trough solar collector type absorber tube, Renew. Energy 108 (2017) 287–302.

[23] A. Elatar, K. Siddiqui, The effect of mixed convection on the structure of channel flow at low Reynolds numbers, Int. J. Heat Fluid Flow 46 (2014) 29–42.

[24] W.L. Lin, T.F. Lin, Experimental study of unstable mixed convection of air in a bottom heated horizontal rectangular duct, Int. J. Heat Mass Transf. 39 (1996) 1649–1663.

[25] C. Chang, X. Li, Q.Q. Zhang, Experimental and numerical study of the heat transfer characteristics in solar thermal absorber tubes with circumferentially non-uniform heat flux, Energy Procedia 49 (2014) 305–313.

[26] F.W. Dittus, L.M.K. Boelter, Heat transfer in automobile radiators of the tubular type, University of California Publications in Engineering, 2 (1930) 443-461.

[27] X. Shen, J. Lu, J. Ding, J. Yang, Convective heat transfer of molten salt in circular tube with nonuniform heat flux, Exp. Therm. Fluid Sci. 55 (2014) 6–11.

[28] J. Dirker, J.P. Meyer, W.J. Reid, Experimental investigation of circumferentially non-uniform heat flux on the heat transfer coefficient in a smooth horizontal tube with buoyancy driven secondary flow, Exp. Therm. Fluid Sci. 98 (2018) 480–496.

[29] X. Fang, F. Zhuang, C. Chen, Q. Wu, Y. Chen, Y. Chen, Y. He, Saturated flow boiling heat transfer: review and assessment of prediction methods, Heat Mass Transf. 55 (2019) 197–222.

[30] A. Kaya, S. Lecompte, M. De Paepe, Experimental Flow Boiling Study of R245a at High Reduced Pressures in a Large Diameter Horizontal Tube, in: Energies, Vol. 15, pp. 864.

[31] J. Bao, L. Zhao, A review of working fluid and expander selections for organic Rankine cycle, Renew. Sustain. Energy Rev. 24 (2013) 325–342.

[32] D.H. Lobón, E. Baglietto, L. Valenzuela, E. Zarza, Modeling direct steam generation in solar collectors with multiphase CFD, Appl. Energy 113 (2014) 1338–1348.

[33] D.H. Lobón, L. Valenzuela, E. Baglietto, Modeling the dynamics of the multiphase fluid in the parabolic-trough solar steam generating systems, Energ. Conver. Manage. 78 (2014) 393–404.

[34] E. Zarza, L. Valenzuela, J. León, K. Hennecke, M. Eck, H.D. Weyers, M. Eickhoff, Direct steam generation in parabolic troughs: Final results and conclusions of the DISS project, Energy 29 (2004) 635–644.

[35] R.K. Pal, K. Ravi Kumar, Two-fluid modeling of direct steam generation in the receiver of parabolic trough solar collector with non-uniform heat flux, Energy 226 (2021), 120308.

[36] Q. Peatiwala, R.D. Boyd Sr., Subcooled flow boiling in circumferentially nonuniform and uniform heated vertical channels with downward flow, J. Heat Transfer 122 (2000) 620–625.

[37] X. Fang, Q. Wu, Y. Yuan, A general correlation for saturated flow boiling heat transfer in channels of various sizes and flow directions, Int. J. Heat Mass Transf. 107 (2017) 972–981.

[38] S. Weise, B. Dietrich, T. Wetzel, Flow-pattern based prediction of flow boiling heat transfer in horizontal tubes with circumferentially varying heat flux, Int. J. Heat Mass Transf. 148 (2020).

[39] M.G. Cooper, Heat Flow Rates in Saturated Nucleate Pool Boiling-A Wide-Ranging Examination Using Reduced Properties, in: J.P. Hartnett, T.F. Irvine (eds.) Advances in Heat Transfer, Vol. 16, Elsevier, 1984, pp. 157-239.

[40] L. Wojtan, T. Ursenbacher, J.R. Thome, Investigation of flow boiling in horizontal tubes: Part II—Development of a new heat transfer model for stratified-wavy, dryout and mist flow regimes, Int. J. Heat Mass Transf. 48 (2005) 2970–2985.

[41] D. Wang, L. Zhao, X. Nie, Y. Lu, S. Deng, Experimental study on flow boiling characteristics of R-245fa in circular tube under non-uniform heat flux, Int. J. Heat Mass Transf. 143 (2019) 118570.

[42] J. Dirker, H. Scheepers, J.P. Meyer, The effect of circumferentially non-uniform heat flux on flow boiling heat transfer in a horizontal tube, Int. J. Heat Mass Transf. 185 (2022), 122428.

[43] J. Dirker, W.J. van den Bergh, H.R. Moran, C.N. Markides, J.P. Meyer, Influence of inlet vapour quality perturbations on the transient response of flow-boiling heat transfer, Int. J. Heat Mass Transf. 170 (2021), 121017.

[44] C.Y. Ho, T. Chu, Electrical resistivity and thermal conductivity of nine selected AISI stainless steels, in, Thermophysical and Electronic Properties Information Analysis Center …, 1977.

[45] K. Cho, S.-J. Tae, Condensation heat transfer for R-22 and R-407C refrigerant–oil mixtures in a microfin tube with a U-bend, Int. J. Heat Mass Transf. 44 (2001) 2043–2051.

[46] I.H. Bell, J. Wronski, S. Quoilin, V. Lemort, Pure and pseudo-pure fluid thermophysical property evaluation and the open-source thermophysical property library CoolProp, Ind. Eng. Chem. Res. 53 (2014) 2498–2508.

[47] L. Wojtan, T. Ursenbacher, J.R. Thome, Investigation of flow boiling in horizontal tubes: Part I—A new diabatic two-phase flow pattern map, Int. J. Heat Mass Transf. 48 (2005) 2955–2969.

[48] T. Wendelin, SolTRACE: A New Optical Modeling Tool for Concentrating Solar Optics, in: ASME 2003 International Solar Energy Conference, Vol. Solar Energy, 2003, pp. 253-260.

[49] R. Charnay, R. Revellin, J. Bonjour, Flow pattern characterization for R-245fa in minichannels: Optical measurement technique and experimental results, Int. J. Multiph. Flow 57 (2013) 169–181.

[50] H.R. Moran, Flow boiling in horizontal pipes: integral measurements, optical diagnostics, and numerical simulations, in: Chemical Engineering, Vol. Doctor of Philosophy (PhD), Imperial College London, Imperial College London, 2021.

[51] M.D. Hoffman, A. Gelman, The No-U-Turn Sampler: Adaptively Setting Path Lengths in Hamiltonian Monte Carlo, Cornell University Library, arXiv.org, Ithaca, 2011.

[52] J. Salvatier, T.V. Wiecki, C. Fonnesbeck, Probabilistic programming in Python using PyMC3., PeerJ Computer Science, 2:e55 (2016).

[53] R.J. Moffat, Describing the uncertainties in experimental results, Exp. Therm. Fluid Sci. 1 (1988) 3–17.

[54] V. Gnielinski, New equations for heat and mass transfer in the turbulent flow in pipes and channels, Int. Chem. Eng. 16 (1976) 359–368.

[55] J.P. Meyer, M. Everts, N. Coetzee, K. Grote, M. Steyn, Heat transfer coefficients of laminar, transitional, quasi-turbulent and turbulent flow in circular tubes, Int. Commun. Heat Mass Transfer 105 (2019) 84–106.

[56] E.N. Sieder, G.E. Tate, Heat transfer and pressure drop of liquids in tubes, Ind. Eng. Chem. 28 (1936) 1429–1435.

[57] J. Liu, J. Liu, X. Xu, Diabatic visualization study of R245fa two phase flow pattern characteristics in horizontal smooth and microfin tube, Int. J. Heat Mass Transf. 152 (2020), 119513.

[58] E. Costa-Patry, J.R. Thome, Flow pattern-based flow boiling heat transfer model for microchannels, Int. J. Refrig. 36 (2013) 414–420.

[59] Y. Zhu, X. Wu, R. Zhao, R32 flow boiling in horizontal mini channels: Part I. Two-phase flow patterns, Int. J. Heat Mass Transf. 115 (2017) 1223–1232.

[60] P. Barbieri, J. Jabardo, E. Bandarra Filho, Flow patterns in convective boiling of refrigerant R-134a in smooth tubes of several diameters, in: 5th European Thermal-Sciences Conference, Eindhoven, The Netherlands, 2008.

[61] H. Canière, B. Bauwens, C. T'Joen, M, Mapping of horizontal refrigerant two-phase flow patterns based on clustering of capacitive sensor signals, Int. J. Heat Mass Transf. 53 (2010) 5298–5307.

[62] C.L. Ong, J.R. Thome, Macro-to-microchannel transition in two-phase flow: Part 1 – Two-phase flow patterns and film thickness measurements, Exp. Therm. Fluid Sci. 35 (2011) 37–47.

[63] G. Sun, G.F. Hewitt, V.V. Wadekar, A heat transfer model for slug flow in a horizontal tube, Int. J. Heat Mass Transf. 47 (2004) 2807–2816.

[64] M.M. Shah, R. Semi-annual meeting of the American Society of Heating, H.T.X.U.S. A.J. Air Conditioning Engineers, Chart correlation for saturated boiling heat transfer: Equations and further study, ASHRAE Trans.; (United States), 88 (1982) 185-195.

[65] S.G. Kandlikar, A general correlation for saturated two-phase flow boiling heat transfer inside horizontal and vertical tubes, J. Heat Transfer 112 (1990) 219–228.

[66] H.R. Moran, D. Zogg, V. Voulgaropoulos, W.J. Van den Bergh, J. Dirker, J. P. Meyer, O.K. Matar, C.N. Markides, An experimental study of the thermohydraulic characteristics of flow boiling in horizontal pipes: Linking spatiotemporally resolved and integral measurements, Appl. Therm. Eng. 194 (2021), 117085.

[67] K.E. Gungor, R.H.S. Winterton, A general correlation for flow boiling in tubes and annuli, Int. J. Heat Mass Transf. 29 (1986) 351–358.

[68] S. Saitoh, H. Daiguji, E. Hihara, Correlation for boiling heat transfer of R-134a in horizontal tubes including effect of tube diameter, Int. J. Heat Mass Transf. 50 (2007) 5215–5225.

[69] Z. Liu, R.H.S. Winterton, A general correlation for saturated and subcooled flow boiling in tubes and annuli, based on a nucleate pool boiling equation, Int. J. Heat Mass Transf. 34 (1991) 2759–2766.

[70] H.-K. Oh, H.-G. Ku, G.-S. Roh, C.-H. Son, S.-J. Park, Flow boiling heat transfer characteristics of carbon dioxide in a horizontal tube, Appl. Therm. Eng. 28 (2008) 1022–1030.